Mitigation of Motion Artifacts in Functional MRI: A Combined Acquisition, Reconstruction and Post Processing Approach

by

Kiran Kumar Pandey

A dissertation submitted in partial fulfillment
of the requirements for the degree of
Doctor of Philosophy
(Biomedical Engineering)
in The University of Michigan
2009

Doctoral Committee:

Professor Douglas C. Noll, Chair
Professor Thomas L. Chenevert
Professor Jeffrey A. Fessler
Research Associate Professor Luis Hernandez
Assistant Research Scientist Scott J. Peltier

ACKNOWLEDGEMENTS

This thesis is the culmination of a journey marked by the hard work, sacrifices, support and guidance of a number of individuals who, over the years, have influenced me in numerous ways and helped me become the person I am today. First, I would like to thank my parents, Sevanand and Trarangini Pandey. Without their tremendous sacrifices, I would not have been able to finish my thesis or, even be able to pursue a graduate education for that matter. This thesis is a result of their constant encouragement, unwavering support and strong faith in me. I would also like to thank my graduate advisor, Dr. Douglas Noll. Doug has been a role model throughout graduate school. He has helped me learn the concepts and provided guidance whenever I needed it. Besides being a wonderful mentor, Doug has also been very patient with me and afforded me freedoms that helped me grow as an individual, beyond a researcher and a doctoral student. I will always appreciate his influence on me. I would also like to thank the other members of my committee: Dr. Jeff Fessler, Dr. Thomas Chenevert, Dr. Luis Hernandez and Dr. Scott Peltier. Their inputs, suggestions, questions, comments have tremendously improved the quality of my thesis. I have also benefitted a lot from my association with them. Thank you!

The members of the fMRI lab have been critical in making me feel at home, away from home during my stay here. Thank you! Keith Newnham, Eve Gochis and Chuck

Nicholas for making life at the fMRI lab “easy” on so many levels. I have also enjoyed great personal and working relationships with all the member s of the fMRI lab: Alberto Vazquez, Bradley Sutton, Sangwoo Lee, Greg Lee, Valur Olafsson, Kelly Bratic, Frank Yip, Christie Kim, Will Grissom, Daehyun Yoon, Hesam Jahanian, Magnus Ulfarsson and many others. I look forward to continuing our association in the future.

Beyond the fMRI lab, I have been blessed by a tremendous group of friends. They have seen me through the lowest of lows and the highest of highs. I cannot put to words the feeling of appreciation and luck that I am overcome with when I think about all of my friends. Finally, I would like to thank God, for all the blessings and good fortune bestowed upon me, perhaps more so than many more deserving individuals in this world. I hope I will use the skills and the opportunities given to me in ways that will benefit the community at large.

TABLE OF CONTENTS

LIST OF TABLES

TABLE:

LIST OF FIGURES

Figure

ABSTRACT

Head motion limits the accuracy, specificity and sensitivity of fMRI. Rigid body registration of fMRI data only corrects for bulk movements while leaving secondary motion artifacts from spin history effects, dynamic field inhomogeneity changes and interpolation errors untouched. Secondary artifacts reduce accuracy of image registration, increase variance in fMRI time-series and reduce sensitivity of detection of active voxels. In this thesis, some approaches to increase robustness of fMRI to head motion have been presented. These involve explicit optimization of acquisition parameters, use of image acquisition and reconstruction methods that reduce secondary motion artifacts and, better isolation and removal of residual motion artifacts that remain after image realignment.

Specifically, methods to mitigate motion artifacts include use of thinner slices and slices of variable thickness during image acquisition for better signal recovery in brain regions with large intra-voxel dephasing induced signal loss. A combined forward and reverse spiral k-space trajectory was used to reduce susceptibility artifacts in presence of motion. Iterative image reconstruction with dynamically updated fieldmaps was used to correct temporally changing field inhomogeneity from motion and susceptibility interactions. Results demonstrated that these corrective measures increased the overall robustness of fMRI to susceptibility induced field inhomogeneity, head motion, and dynamic interactions between them. Consequently, better quality of fMRI data also improved the quality of motion correction, reduced variance in the time-series and

increased sensitivity of detection of active voxels during fMRI experiments with head movement.

Constrained Independent Component Analysis (cICA) was used for modeling, isolation and removal of residual motion artifacts that remain in fMRI time-series despite image registration. cICA was found to be better able to isolate the residual errors compared to the prevalent General Linear Model (GLM) methods. Further, cICA automated the identification and removal of erroneous components and eliminated human errors during this process. Using a combined approach, i.e., by optimizing acquisition parameters, acquisition methods, and reconstruction methods during data collection to improve image quality and motion correction and, by better modeling, isolation and removal of residual motion artifacts using cICA, the impact of head motion on fMRI studies can be vastly reduced.

CHAPTER 1

Introduction - Motion in Functional MRI

1.1 Motivation

Head motion is a significant confound in functional Magnetic Resonance Imaging (fMRI) as it degrades the accuracy, specificity and sensitivity of the study. Movement during fMRI violates the assumption that **change in pixel intensity at any spatially fixed brain location is solely due to change in functional state of the tissue** [1-5]. Head motion causes erroneous intensity changes in fMRI dataset and introduces unwanted image artifacts via multiple mechanisms. Primary motion artifacts such as gross head movements lead to blurring of images and, streaking and banding artifacts [6]. Even sub-millimeter task correlated movements under the right circumstances can cause erroneous intensity modulations similar to task induced functional contrast [1, 2], while task uncorrelated motion increases variance in fMRI data.

In addition to the primary artifacts, head movement during acquisition of images in the fMRI time-series might cause prominent "secondary" artifacts. One major source of secondary artifacts is the motion induced dynamic changes in magnetic field inhomogeneity at the susceptibility mis-matched air/tissue/bone interfaces in the brain [7-9]. Movement between scans, especially in 2D planar fMRI, might lead to displacement

of the object in the scanner reference frame and cause excitation of a different slice volume at subsequent time points in the fMRI time series. This process leads to the "spin history" effect, another major source of secondary artifacts in fMRI [2]. Image registration, a commonly employed corrective measure for head motion, introduces errors in the data due to inaccurate interpolation and is yet another source of secondary artifact [10, 11]. Interactions between head motion and orientation dependent artifacts cause complex and unpredictable patterns of signal loss, intensity fluctuations, saturation profile related "spin history" effects, and distortions in MR images. Corruption of fMRI data in this manner reduces the accuracy of the image registration, increases variance in voxel time-series and potentially leads to false activations. Thus, primary and secondary motion related artifacts limit the effectiveness of fMRI as a neuro-imaging tool.

Motion correction in fMRI consists of rectifying mostly primary motion artifacts via image registration. Current motion correction algorithms use a rigid body or affine transformation to register motion-corrupted images to a reference image by optimizing an intensity based cost function that penalizes image dissimilarity [12-17]. Under optimal conditions of small movement and no (or small) secondary artifacts, image registration algorithms can be very accurate. However, for a variety of logistical reasons and, in fMRI studies involving patients with neuro-psychological disorders, large head movement is not preventable during fMRI experiments. In presence of large head motion, the accuracy of the image realignment step might be significantly reduced. This is because the secondary artifacts, which are usually ignored during realignment, might cause the images in the fMRI time-series to be structurally dissimilar from each other beyond just a rigid body or affine reorientation in the scanner coordinates.

Off-resonance artifacts caused by susceptibility/motion interactions induced dynamic field inhomogeneity degrade fMRI data in a manner that can be complex, non-linear and unpredictable or difficult to model [7]. Spin history effects and interpolation artifacts further degrade the images in the time series. In this context, improvements to the accuracy of realignment methods and increasing the robustness of fMRI to harmful effects of head motion depend on successfully accounting for secondary artifacts in fMRI dataset.

In this thesis, I have presented some methods to reduce the motion related secondary artifacts in fMRI and remove the residual motion artifacts left after image registration. First, the ability of many acquisition parameters, acquisition methods and reconstruction methods to increase the robustness of fMRI to off-resonance artifacts from susceptibility induced field inhomogeneity and its interactions with head motion were investigated. Use of the optimal parameters, acquisition and reconstruction methods thus identified improved the quality and fidelity of images in fMRI time series and also, the accuracy of image registration. Better quality of images and more accurate image registration reduced variance in the fMRI time-series and improved sensitivity of detection of functionally active voxels. Effective post-processing methods were developed to model and remove residual motion artifacts that remain after image registration and are ignored during data processing steps currently used. The topics covered in this thesis can be summarized as follows:

1. **Analysis of the effect of acquisition parameters and acquisition methods on quality of motion correction.** The use of optimal **acquisition parameters** – slice thickness / sampling or spacing / orientation / profile, and **acquisition**

methods reversed spiral (spiral-in), forward spiral (spiral-out) and combined forward and reversed spiral (spiral-in-out), and variants – were investigated for their ability to make images robust to susceptibility induced off-resonance artifacts in presence of motion. Reduction of these off-resonance artifacts resulted in higher fidelity of fMRI data and lead to more accurate image realignment consequently, higher overall accuracy and sensitivity of fMRI studies.

2. **Application of model-based iterative image reconstruction with joint estimation of dynamic fieldmaps and correction of susceptibility induced artifacts arising from head movement.** Iteratively reconstructed images based on physics based models approximate the MR imaging process more accurately than the Fourier reconstruction methods. Use of dynamically updated fieldmaps during image reconstruction might better correct image artifacts from temporally changing off-resonance patterns that arises from interactions between head motion and susceptibility induced field inhomogeneity. Iterative image reconstruction with dynamic field maps significantly improved the quality and accuracy of reconstructed images corrupted by motion and increased the robustness of fMRI studies to head motion induced artifacts.

3. **Develop post processing methods to estimate and correct for signal variation resulting from incomplete head motion correction as well as artifacts from registration/reslicing processes.** Residual artifacts that remain after image

registration, especially structured noise due to head motion and its secondary effects were modeled and removed. Semi-blind source separation methods that use constrained Independent Component Analysis (cICA) [18] to isolate erroneous components were used for modeling and removal of these residual artifacts. Motion parameters from the registration step were used as the reference. Modeling and removal of residual errors might reduce the amount of unmodeled variance present in the fMRI time-series and lead to improved sensitivity of detection of active pixels.

1.2 Functional MRI

fMRI uses serially acquired MR images of the brain to create structure/function maps and explore neuropsychological and cognitive principles underlying brain function [19-22]. Due to its increasing prevalence and accessibility, fMRI is also being used to diagnose nervous pathology and as a neurosurgical mapping/delineation tool [23]. The viability of fMRI was first demonstrated using an external contrast agent to track changes in cerebral hemodynamics during cortical activation [24]. Over the years, several techniques have been developed that do not require contrast agents, making fMRI a truly non-invasive procedure. Some of the fMRI techniques employed at present use susceptibility based contrast (e.g., Blood Oxygen Level Dependent, BOLD) [20, 25], perfusion based contrast (e.g., Arterial Spin Labeling, ASL) [22, 26, 27], cerebral blood volume based contrast (e.g., vascular space occupancy (VASO) [28]) and others for detection and localization of neuronal function.

1.3 BOLD fMRI

BOLD fMRI is the most widely used fMRI technique due to its higher SNR, better sensitivity and higher temporal resolution that allows detection of activation from single events [19, 29]. The BOLD fMRI technique uses T_2* weighted images to track oxygenation level dependent changes in magnetic susceptibility of hemoglobin in red blood cells. In the oxygenated state, hemoglobin in the red blood cells is slightly diamagnetic with susceptibility similar to that of surrounding tissue while in the deoxygenated state, hemoglobin is strongly paramagnetic. Thus, presence of oxygenated hemoglobin leads to a comparably more uniform local magnetic field environment and, excess deoxygenated hemoglobin distorts the field due to its paramagnetic property. This behavior can be explained in terms of T_2*, an MR imaging constant that characterizes the rate of MR signal decay. Presence of field inhomogeneity or distortions cause dephasing of the spins and lead to faster signal loss (shorter T_2*) compared to spins in a more uniform field environment (longer T_2*). Presence of excess deoxygenated hemoglobin results in a shorter T_2* and signal loss. Correspondingly, excess oxygenated hemoglobin leads to a longer T_2*. This is the contrast mechanism used by BOLD fMRI.

During "neuronal activation", there is a focal increase in metabolic demand in brain regions in close proximity to neurons that are active in response to a provided external stimulus. To address this need, there is an increase in cerebral blood flow (CBF), cerebral blood volume (CBV), oxygen metabolism and extraction ($CMRO_2$) to the affected region. However, this increase in vascular supply is proportionately much higher than the existing demand and leads to an excess of oxygenated blood in the brain vasculature and tissue surrounding the site of neuronal firing. Oxy-hemoglobin rich

environment leads to an increase in T_2* and a net signal increase [19, 20, 30]. During a BOLD fMRI study, the subject is asked to perform a task and the neuronal response to the task is monitored by tracking the functionally induced changes in T_2* weighted time-series of MR images. The T_2* of the "active" regions increases due to mechanism described above and can be identified as the part of the brain responsible for the response elicited by the stimulus provided.

Although widely used, BOLD fMRI has a number of shortcomings. BOLD is an "indirect" method for tracking the primary event, the neuronal activation, via observation of a secondary event or the hemodynamic response to the primary event. The underlying physiological mechanism of BOLD has not yet been fully characterized. Suggestions of non-linearity of the underlying neuro-vascular coupling limits the validity of inferences drawn from various fMRI studies which assume a linear model for BOLD [31].

Besides the ones listed above, BOLD has another set of limitations which have been investigated in this thesis. BOLD uses susceptibility contrast or T_2* weighting for detecting functional activation. This makes it vulnerable to bulk susceptibility artifacts and their dynamic interactions with head movement. Fast, single shot acquisition methods namely, Echo Planar Imaging (EPI) and spiral methods, are themselves susceptible to off-resonance effects because these methods use longer acquisition times. Although, BOLD Signal to Noise Ratio (SNR) increases at higher fields, the susceptibility artifacts become more prominent as well [32].

Despite a long list of limitations, BOLD fMRI is better able to characterize brain activation compared to competing methods. Given the prevalence of BOLD fMRI,

development and use of methods that increase robustness of BOLD fMRI to susceptibility artifacts and its interaction with head motion will be critical in improving and extending the capabilities fMRI as an effective neuro-imaging tool. The development of such robust BOLD fMRI methods is the major focus of this work.

1.4 Motion in fMRI: Artifacts

Head motion is a prominent confound in fMRI that has commanded a lot of attention and resources within the community. Given its adverse effects of fMRI, prevention of head motion altogether would be ideal. However, the long duration of scan sessions and the restrictive environment inside the MRI scanner make it impossible to eliminate head motion despite use of immobilization devices and methods such as physical restraints, bite bars, padding and head molds, visual feedback systems [33]. Further, use of most motion prevention methods does not preclude effects of small head movement from physiological process like swallowing, breathing, speech, pulsation from blood flow. Currently, most investigators include motion correction as an essential pre-processing step before statistical analysis of fMRI datasets. Some of the types of motion artifacts and their underlying mechanisms are detailed below:

1.4.1 Primary Motion Artifacts

Primary motion artifacts mostly include direct undesirable effects from gross movement of the object in the scanner reference frame. The fMRI community treats bulk movement of the head as a rigid body motion characterized by six degrees of freedom - three rotation parameters, Rx, Ry, Rz (rotations around the x, y, z axis) and, three

translation parameters, Tx, Ty, Tx (translations in the x, y, z) respectively. Bulk motion can lead to blurring of images, banding and streaking artifacts [6] and reduce spatial resolution [3, 34]. Bulk movement, when correlated to task, can also lead to spurious activations. Consider an anecdotal case of an isotropic fMRI voxel, dimension: 4 mm, at the edge of the brain or at a high contrast tissue/air interface. In fMRI experiments, activation induced signal changes range in between 1%-10%. Thus, for the example 4mm voxel, a 400 μm shift of the head that is correlated to the task can lead to a 10% change in signal intensity caused by bleeding of the brighter voxel into the domain of the darker voxel and vice versa. Such intensity fluctuation could easily (and falsely) be interpreted as functional contrast. Thus, task-correlated motion results in erroneous signal indistinguishable from the true signal and reduces specificity of fMRI as demonstrated by Hajnal et. al. [1]. On the other hand uncorrelated head motion adds erroneous intensity fluctuations and increases the variance in a voxel's time series thereby reducing the sensitivity of detection.

Further, image registration, a corrective measure for primary motion artifacts, itself might be a source of additional errors in the fMRI dataset. Activation induced localized changes in image intensity have been implicated in biasing estimates of motion parameters and lead to inaccurate image realignment and corrupt fMRI data. Algorithms using a minimum squared error based cost function are especially vulnerable in this regard [4]. Registration also introduces interpolation errors into the time-series [10, 11].

1.4.2 Secondary Motion Artifacts

Secondary motion artifacts are more localized in their effect yet their impact can be just as adverse as primary motion artifacts. Some of the secondary motion artifacts and their mechanisms are discussed below.

Artifacts from interactions between motion and susceptibility

The non-uniform magnetic field, be it due to system based inadequacies such as erroneous shimming of B_0 field or patient specific field inhomogeneity at interfaces of differing susceptibility, causes off-resonance artifacts: signal loss and distortions that severely degrade MR images. With head motion, the pattern and effects from field inhomogeneity, most notably from the susceptibility mismatched interface between tissue air/sinuses, change orientation and lead to unpredictable signal loss and image distortion in subsequent images in the time-series. These image artifacts prevent registration and transformation algorithms from working properly and add to the variance in the image time-series. Susceptibility induced field inhomogeneity manifests itself in signal loss or image distortions both of which contribute to secondary artifacts. Their mechanisms are elaborated below.

SIGNAL LOSS: In BOLD fMRI, acquired images are T_2* weighted to obtain maximum BOLD contrast. As such, the echo time (TE) during image acquisition is fairly long to allow for the evolution of this contrast. However, as depicted in **figure 1-1**, use of longer TE to allow for evolution of T_2* contrast increases the intra-voxel dephasing, mostly from undesirable erroneous field gradient in the through-plane and results in signal loss/voids prominent near the sinuses and air/tissue interfaces [36]. Many of the brain regions affected by signal voids are responsible for control and coordination of important

task. Signal voids from intra-voxel dephasing might prove to be a significant hindrance in those fMRI studies. Further, signal loss can be caused by the presence of in-plane susceptibility gradients that cause shifting and skewing of the k-space trajectory and prevent the measurement of signal near the center of k-space [37].

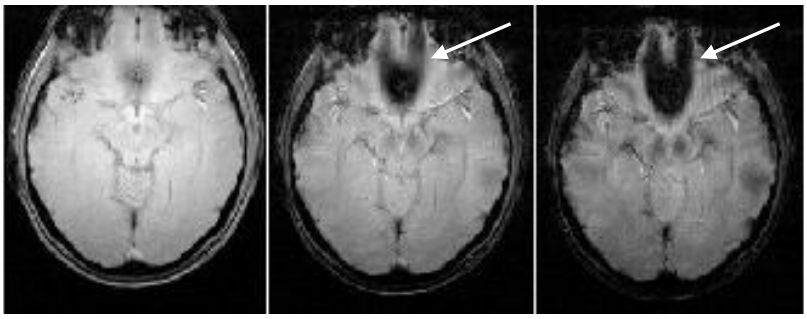

Figure 1-1: Images of the same object acquired at TE = 10 (left), 20 (middle), 30 (right) ms respectively. The signal loss due to intra-voxel dephasing near the sinus gets progressively worse with increasing TE as indicated by the increasing size of the signal void. Also, the blurring and piling artifacts become more prominent at higher TE (highlighted by arrows).

IMAGE DISTORTIONS: Magnetic field inhomogeneity is responsible for distortion and blurring of images acquired with EPI and spiral acquisition methods respectively [38-40]. Susceptibility mismatch induced first order in-plane field gradients especially near tissue-air interfaces add to image distortions by skewing the k-space trajectory in addition to signal loss from inadequate sampling of low frequency region in k-space. This effect will be further explored in chapter 3 of this work.

Finally, examination of spatial maps of residual variance after motion correction can point to sources of error in motion correction algorithms. **Figure 1-2** contains an image of residual variance for a sagittal slice near the midline. From this image, we can

see that the highest variance area lies in the region of susceptibility artifact directly above the sphenoid sinus, as indicated by the arrow thus providing further confirmation to the importance of addressing movement-susceptibility interactions that lead to residual variance in fMRI data even after image realignment.

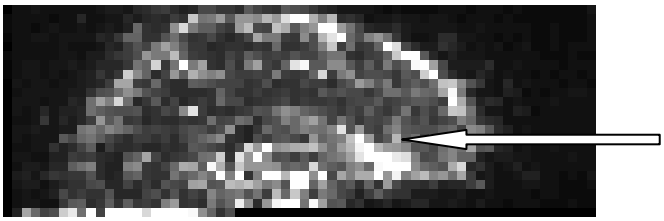

Figure 1-2: For a representative image after motion correction, the variance map shows relatively large values (brighter regions) near the sinuses (arrow) and edges.

Inadequate Slice Sampling

A spectral approach to analysis of the slice selection process in 2D planar MRI was used by Noll et. al. [10] to show that the inherent undersampling of image volume in the slice-select direction might be a source of interpolation errors during image registration in 2D planar fMRI. This undersampling in the through plane direction causes aliasing errors during motion estimation and reslicing step of image realignment. While the use of 3D imaging methods can circumvent these issues, due to desired high temporal resolution, 2D planar imaging continues to be the method of choice for functional imaging studies.

Image registration steps introduce additional residual variability into the image data due to improper interpolation, especially when reslicing the images to sub-pixel dimensions. In interest of time, motion correction schemes use a suboptimal interpolation

kernel and other sub-par filter designs to reslice the data into the reference image coordinates. Although most of the in-plane motion can be fairly accurately accounted for by using Fourier domain registration methods [41] and also because the data is adequately sampled in-plane, the sub-pixel movements in the slice select direction involve a data interpolation step that might result in inaccurate registration and introduction of an artificial variance [11]. The residual interpolation artifacts can be correlated to motion and in a scenario where motion is correlated to the stimulus; these artifacts can potentially significantly alter the specificity and sensitivity of fMRI experiments.

Spin History Effect

Another source of residual errors is the "spin history effect" [2]. Generally, fMRI studies involve repeatedly imaging a 3D region of interest in the brain by acquiring many sequential 2D image slices that are either contiguous or have boundaries at close proximity. The assumption is that the brain volume remains stationary between subsequent acquisitions such that every 2D slice images the same brain region throughout the entire scan. However, motion during the scan might change the spin saturation profile within an imaged 2D slice. For example, motion might cause saturated spins from slices that were imaged just prior to the current slice to move into the space of the current slice prescription thereby reducing the intensity of acquired images, especially near the edges. Friston et. al. [2] have done detailed modeling and analysis of this effect and have concluded that spin history might be a major source of error in an fMRI experiment especially at shorter TRs. For most fMRI experiments however, adequate choice of TR can minimize this effect.

Besides the ones listed above, there are quite a few other mechanisms that contribute to head movement induced artifacts including artifacts from intra-volume motion, changes in effective coil sensitivity profiles, especially during parallel imaging that need to be effectively addressed, beyond a simple image registration step, in order to increase the accuracy of the realignment step and fidelity of fMRI studies.

1.5 Motion Correction & Limitations of Existing Techniques

Given its adverse effects on fMRI, it is highly desirable to prevent head motion altogether. Despite restraining systems and considering the restrictive environment inside the scanner, small head motions would be hard to prevent and, in most cases, cause major patient discomfort. In fact restraining systems might perpetrate head motion by causing subjects to adjust head position to relieve awkward pressure points. As such image registration has become an indispensable pre-processing step for almost all fMRI studies.

1.5.1 Image Registration

Currently, investigators include motion correction as an essential pre-processing step before statistical analysis of fMRI datasets. Typically, motion correction in fMRI includes a retrospective image realignment step to correct for bulk head movement during the scans. Image registration packages use an iterative rigid body or affine transformation to estimate motion parameters via optimization of a similarity (usually intensity) based cost function and register or reslice the displaced images to coordinates of a reference image using these parameters [12-16, 41, 42].

Limitations: The realignment algorithms can achieve sub-millimeter accuracy under ideal conditions; however, in presence of large head motion, their effectiveness is limited by image quality, robustness of optimization methods used and interpolation artifacts during image registration. Registration accuracy and fMRI sensitivity is further compromised in presence of secondary artifacts that are a function of the head orientation and movement. In presence of secondary artifacts, the assumption of inter image similarity might be inaccurate. Thus the accuracy of parameter estimation step and consequently, the overall completeness of image registration itself might be reduced. Two prominent artifacts already discussed in this context are "spin history" artifacts [2] and susceptibility artifacts that induce signal loss, intensity modulation and image distortion [7]. In many fMRI studies, activation related intensity changes in images – during task versus control periods - might bias motion parameter estimation and prevent image registration from working properly [4]. Moreover, as previously stated, registration itself leads to interpolation artifacts during the estimation of motion parameters as well as the reslicing step.

While the effect of "spin-history" is usually minimal at longer scan repetition times, typical of fMRI experiments, the characterization and correction of susceptibility artifacts and their interaction with head motion during fMRI poses a real challenge and will be investigated in detail during the course of this work.

1.5.2 Navigator Echoes

To correct for motion in real time and to prevent interpolation artifacts, several prospective motion compensation methods have been developed. One notable group of methods use navigator echoes to freeze head orientation relative to the scanner

coordinates by constantly tracking and updating the location of imaged slice or volume at each time point [43-46]. The images thus acquired do not need to be registered retrospectively and are potentially immune to residual movement related "spin-history" effects.

In interest of shortening the scan repetition times, the additional scans required to estimate the inter-volume movement can be supplanted by measurements from an independent external motion tracking device. The tracker updates the motion parameters in real time and facilitates prospective re-prescription of the volume to be imaged in a manner similar to traditional navigator echo methods [47, 48]. Besides better temporal resolution, use of external tracking methods might improve accuracy of motion estimates as the image based motion parameter estimates might be biased due to motion dependent susceptibility artifacts. Of course, the estimated motion parameters from the navigator echoes can also be used to do retrospective image realignment.

Limitations: The markers for external monitoring are attached to the skull externally and might not accurately track the motion of the brain itself. Further, despite their advantages, navigator echo and external tracking methods do not compensate for susceptibility artifacts and their interactions with motion. Thus secondary artifacts will remain in the dataset and increase variance in the time series ultimately leading to reduced specificity and sensitivity of fMRI studies. Additional measures are necessary to increase robustness of fMRI studies to these artifacts, especially in presence of large head motion.

1.5.3 Other Methods for Motion Correction in fMRI

Thus far, we have considered inter-volume head motion only. Impulsive motion can occur in between acquisition of slices and during acquisition of a single slice. In case of intra-volume motion, images before movement will be structurally similar to data acquired prior to the motion and the slices acquired after the movement might register better with subsequent volumes. In such a case, identification and exclusion of data might be a simplistic remedy, although, approaches such as slice to volume registration methods by Kim et al, [49] in which an individual slice is registered to a reference volume might be a more complete solution. The slice to volume registration technique suffers from its own set of troubles, namely, some of the image volumes have voids due to displacements/registration of slices to a different anatomical volume (in the reference image) than at the location that they were acquired, thus leading to potential issues with statistical parameter estimation.

Other approaches to motion correction in fMRI datasets include use of different image acquisition trajectories that are inherently robust to motion, for example, spiral, projection imaging [34, 50]. Further, use of PROPELLER [50], fiducial makers [51] for retrospective registration and prospective online methods [52] are a few of the other major initiatives to mitigate the effects of head motion during fMRI. Despite their advantages, all of these methods do not correct for the secondary artifacts; as such, their effectiveness is always limited.

1.6 Motion Correction: Proposed Improvements

In the sections below, a few of the methods to improve motion correction and robustness of fMRI studies to large motion by alleviating artifacts from secondary sources are proposed. More specifically, we will optimize the acquisition, reconstruction and post processing methods to reduce vulnerability of MR images to susceptibility effects and other sources of secondary artifacts. Increasing the fidelity of images in presence of these errors will improve image registration and increase the sensitivity and specificity of fMRI studies.

1.6.1 Optimal Slice Thickness/Orientation/Profile

Reducing slice thickness for fMRI has a two-fold advantage. First, it reduces signal loss from intra-voxel dephasing by limiting the extent of dephasing from inhomogeneous field gradients [36, 53]. Second, thinner and contiguous slices increase data sufficiency and reduce aliasing error in the through plane direction by better sampling of the imaging volume. They also prevent propagation of errors from under-sampling during each motion estimation and reslicing steps [10]. Use of slice profiles with narrower spectral content and optimal interpolation kernels further reduce through plane aliasing errors. Use of thinner and contiguous slices require additional data acquisition and increases scan time while lowering SNR, both of which might not be desirable in fMRI studies. To alleviate this issue, a variable slice thickness acquisition scheme can be used where the minimally affected higher brain regions are acquired with thicker slices while the lower regions near the sinuses are acquired with thinner slices. This may significantly improve the image signal recovery in the lower regions of the brain at a minimal temporal penalty and SNR penalty.

1.6.2 Use of Forward and Reverse Acquisition Trajectories

In plane signal loss and distortions of k-space can also be explained using the concept of local k-space [54]. The susceptibility induced in-plane field gradients causes shifting and skewing of k-space resulting in signal loss by inadequate sampling of the low frequency region in k-space. Acquisition methods such as time-reversed spiral (spiral-in) acquisitions preserve more signal than standard forward spiral (spiral-out) or echo-planar imaging (EPI) and increase the image SNR even in presence of significant *first order variable field in-homogeneity*. Improved image quality with reversed spiral can potentially improve motion correction. Combination of forward and reverse spiral acquisition scheme may enable better activation detection by combining the advantages of the respective acquisition schemes, better motion correction due to higher SNR and low signal loss for images with reverse spiral and better BOLD sensitivity to T2* weighted activation detection.

1.6.3 Iterative Image Reconstruction & Use of Dynamic Fieldmaps

In MRI, Fourier-based reconstruction methods have been predominant because of computational advantages of FFT even though they do not accurately model the MR imaging process as effects of field inhomogeneity; relaxation, etc. are not included. Some methods explored are: conjugate phase reconstruction with different robust k-space trajectories [40] and iterative physics based image reconstruction with jointly estimated and dynamically updated fieldmaps [55, 56]. Iterative reconstruction with dynamically updated fieldmaps is better able to model and correct for inhomogeneity induced off-resonance effects due to head motion and are not limited by design and of complicated density compensation functions or smoothness of fieldmaps as in case of conjugate phase

or other FFT based reconstruction. Use of iterative reconstruction and dynamic fieldmaps might increase the fidelity of images in the time series and the quality of motion correction.

1.6.4 Constrained ICA – Modeling and Removing Residual Motion Artifacts

Some prominent sources of error in fMRI data are: rigid body or affine displacement, susceptibility induced field inhomogeneity related artifacts and its interactions with head motion, interpolation errors during registration, impulsive or intra-slice and intra-volume movement, spin-history effects. Despite registration, motion artifacts still persist in the time series data. This fact has been supported by increased statistical power of detection from modeling and whitening approaches that removed structured noise [57, 58]. Structured noise can be removed by including models of noise contributions as nuisance variables in the design matrix of the data processing step and then regressing them out of the fMRI dataset [59]. However, the success of such modeling approaches for removal of motion errors depends on the accuracy of the noise model (physiology, off-resonance, motion etc) used in the General Linear Model (GLM) method. In most cases there is an opportunity for further improvement as the current noise models are an approximation and do not capture the full range of variability or error introduced by the respective noise/artifact source. For example, many investigators currently use motion parameters as nuisance variables and have reported reduced residual error post registration and improved detection power [59]. In case of large head movement or interpolation artifacts and incomplete off-resonance correction, linear models are unable to capture the erroneous contributions from such potentially non-linear sources. As a part of our post-processing, we have used semi-blind source separation

(semi-BSS) methods such as constrained ICA (cICA) [18, 60, 61] to extract these unmodeled or inadequately modeled erroneous components in fMRI data and investigate their effect on the quality of detection of relevant voxels. In case of the cICA, the separated components have some inherently desirable properties, for e.g., the isolated components are statistically independent yet, use of a reference or some other prior information regarding the expected structure of the component constrains the final output to be similar to a reference [61]. As an example of use of our proposed method, it is quite possible to utilize knowledge of motion parameters or alternatively some geometric model of interpolation artifacts based on motion parameters and isolate linear and non-linear contributions from interpolation artifacts using cICA methods.

CHAPTER 2

Acquisition Parameters – 2D Slice Characteristics

2.1 Background and Theory

As stated before, one of the goals of this work is to optimize MRI acquisition parameters to make fMRI robust to large head motion. After an initial exploration of effect of various acquisition parameters on robustness of fMRI to head motion namely, TE, image resolution and others, the benefits from optimizing slice parameters seemed most promising. The advantage of using optimal slice parameters during image acquisition is two-fold. First, use of proper choice of slice thickness (in this case thinner slices) will mitigate the extent of signal loss and increase robustness to susceptibility via motion artifacts. Second, use of appropriate thickness, spacing, slice profile and orientation might be critical in reducing interpolation errors during parameter estimation and realignment steps of image registration. Based on our study of benefits of using thinner slices for image acquisition in 2D planar fMRI studies, we further developed a new acquisition method which sampled the 3D volume using 2D planar slices of variable thickness in the through plane direction. This method exploits the advantages from use of thinner slices while decreasing the loss in temporal resolution from use of thinner slices. Important aspects of our work are elaborated in the sections below.

2.1.1 Reducing Susceptibility Artifacts in fMRI using Thinner slices

The first advantage of reducing slice thickness during image acquisition in fMRI is that thinner slices decrease signal loss from intra-voxel spin dephasing by limiting the net spatial extent of inhomogeneous field gradients in the slice select direction [36, 53]. The inhomogeneous field patterns in consideration here are especially prominent at regions of susceptibility mismatch such as the interfaces of brain tissue and sinuses.

The MR signal equation for imaging a 3D volume in presence of field inhomogeneity, $\Delta B_0(r)$ can be stated as:

$$\textbf{(2.1)} \quad s(t) = \int_V f(r) e^{-i\gamma \Delta B_0(r)(t+T_E)} e^{-i2\pi(k(t).r)} dr$$

where, $s(t)$ is the signal received at instant t from object V, a 3D volume of interest, and $k(t) = [kx(t),\ ky(t),\ kz(t)]^T$ is the the k-space trajectory. Assuming the commonly used framework of multi-slice 2D planar imaging of 3D objects, the 3D volume of interest can be separated into the product of a 2D image in the x, y plane, $I(x, y)$ and a slice profile in the z plane, $p(z)$. The signal equation **2.1** can now be represented as:

$$\textbf{(2.2)} \quad s(t) = \int_{x,y} \int_z I(x,y) p(z). e^{-i\gamma \Delta B_0(r)(t+T_E)} e^{-i2\pi(k_x(t)x + k_y(t)y)} dz\, dx dy.$$

After Taylor expansion of the inhomogeneity, $\Delta B_0(r)$, and ignoring the higher order terms beyond the first, one obtains:

$$\textbf{(2.3)} \quad \Delta B_0(r) \approx \Delta B_0(x,y) + g_z(x,y).(z - z_0)$$

Where $\Delta B_0(r)$ and $g_z(x,y)$ are the zeroth order (mean) and first order (gradient) frequency offset at location x,y respectively. Substituting equation **2.3** into equation **2.2** and rearranging the terms leads to:

$$\textbf{(2.4)} \quad s(t) = \int_{x,y} [\int_z \underbrace{p(z - z_0).\, e^{i\gamma g_x(x,y)(z-z_0)(t+T_E)}\, dz}_{l(x,y,t)}] \, I(x,y) \; . \underbrace{e^{-i\gamma \Delta B_0(x,y)(t+T_E)}}_{\Phi(x,y,t)} e^{-i2\pi(k_x(t)x + k_y(t)y)} dx dy.$$

$l(x,y,t)$ quantifies the signal loss via through-plane dephasing due to the gradient offset and, $\Phi(x,y,t)$ quantifies the phase offset due to the mean deviation of the local magnetic field. In case of the commonly used rectangular slice profile of thickness Δz, the signal loss at TE or when the k-space center is sampled can be shown to be:

$$\textbf{(2.5)} \quad l(x,y,0) = \int_{z_0 - \frac{\Delta z}{2}}^{z_0 + \frac{\Delta z}{2}} e^{i\gamma g_x(x,y)(z-z_0)(0+T_E)} dz = sinc\left(\frac{\gamma \Delta z g_z(x,y) T_E}{2}\right).$$

Thus, the received signal intensity in presence of a through plane gradient $g_z(x,y)$ depends on TE and slice thickness, Δz. In functional imaging, the TE is usually fixed and set equal to the T_2* parameter for maximum functional contrast. By reducing the slice thickness in the 2D planar acquisition scheme, one can reduce the net dephasing across a given voxel and consequent signal loss however, at the cost of increasing the number of slices to cover volume of interest.

2.1.2 Effect of Slice Spacing, Profile, Orientation: A Spectral Perspective

In their detailed study of the slice selection process in 2D planar fMRI from a spectral perspective, Noll et. al., [10] have shown that use of thinner and contiguous slices, slice profiles with narrower spectral content and use of sophisticated interpolation kernels reduce through plane interpolation errors. Considering the fact that data interpolation is an integral part of the image registration, a closer look at some of the ways of reducing this artifact might be highly beneficial.

To briefly recap the major points of the study cited above, in most fMRI studies the 3D volume is sampled via multiple 2D planar slices. In 2D planar imaging, acquired image, $\mathbf{m_s(z)}$, can be represented as a convolution of the original object to be imaged, $\mathbf{m(z)}$, by the slice profile, $\mathbf{s(z)}$ followed by sampling of the smoothed image at the slice locations, $\mathbf{W}$. This is mathematically represented as:

$$\mathbf{(2.6)} \quad m_s(z) = [m(z) * s(z)] \sum_n \partial(z - nW)$$

Using principles of signal processing, the above process can be represented in the spectral domain, as:

$$\mathbf{(2.7)} \quad M_s(k_z) = [M(k_z)S(k_z)] * \frac{1}{W}\sum_n \partial(k_z - \frac{n}{W})$$

where, $\mathbf{M(k_z)}$ is the spatial frequency spectra of the original object, $\mathbf{M_s(k_z)}$, is the spectra of the object after smoothed by the slice profile and sampled at the respective slice locations. As the object being imaged is inherently undersampled in the through plane direction, $\mathbf{M_s(k_z)}$ is in fact the spectral representation of the original object contaminated with aliasing errors as shown in **figure 2-1**.

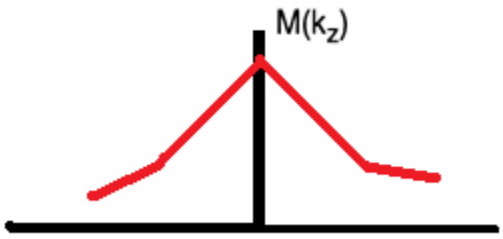

Figure 2-1a: Spatial frequency spectra of the original object.

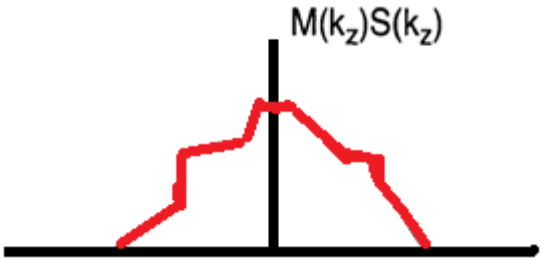

Figure 2-1b: Spatial frequency spectra of the object convolved with the slice profile.

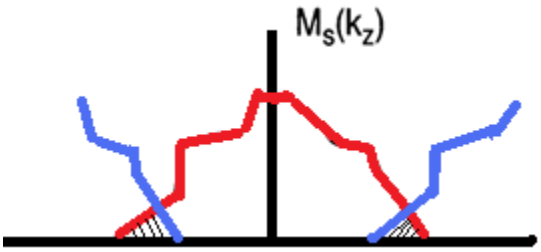

Figure 2-1c: Spatial frequency of the slice-sampled object. The shaded regions represent the aliasing error due to inadequate sampling of object in through-plane direction

Figure 2-1: The slice selection process in the spectral domain. (**Adapted from reference [10]**)

In the signal processing context described above, contiguous slices improve sampling compared to sampling of the object of similar thickness but, with gaps between them. Also, slice profiles with lower extent spectral content $\mathbf{S(k_z)}$ will, in effect, reduce the amount of aliasing by limiting the extent of the spectral frequencies in $\mathbf{M_s(k_z)}$. Interpolation process can be described as an estimate of the object shifted by $\mathbf{z_0}$, and can be approximated by convolution of the sampled object, $\mathbf{m_s(z)}$ with an interpolation kernel, $\mathbf{c(z)}$:

(2.7) $$\mathbf{m}_{s,z_0}(z) = [m_s(z) * c(z - z_0)] \sum_n \partial(z - nW)$$

In the spectral domain, this can be represented as:

(2.8) $$\mathbf{M}_{s,z_0}(k_z) = \left[M_s(k_z) C(k_z) e^{i2\pi z_0 k_z}\right] * \frac{1}{W} \sum_n \partial(k_z - \frac{n}{W})$$

The spectra of the original object are given by:

(2.9) $$\mathbf{M}_{s,z_0}(k_z) = \left[M_s(k_z) S(k_z) e^{i2\pi z_0 k_z}\right] * \frac{1}{W} \sum_n \partial(k_z - \frac{n}{W})$$

There are two sources of error that one needs to consider during interpolation. First, unless one uses an infinite "sinc" for $\mathbf{c(z)}$, (in which case, $\mathbf{C(k_z)}$ is a "rect") the interpolation kernel, the spectra after the interpolation step will be inaccurately weighted down by the kernel itself and this might lead to erroneous recreation or estimation of the interpolated data. This effect is depicted in the **figure 2-2a** where the original spectrum is the gray line and the darker trace represents the modified spectra after interpolation. As can be seen, the original spectrum is weighted down by the interpolation kernel itself.

Second, the resampling of the interpolated image will give rise to more aliasing and result in accumulation of error for each new interpolation step as shown in the **figure 2-2b.** If left unchecked, these interpolation errors might compound during the estimation of parameters and reslicing - which are carried out multiple times during parameter estimation and reslicing step of image registration – and lead to prominent image artifacts.

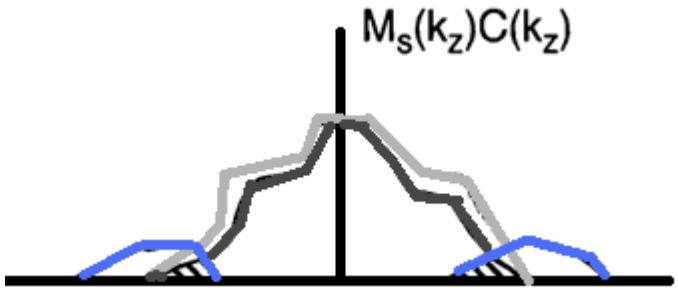

Figure 2-2a: The gray line represents the original spectra while the black outline represents the modified spectra weighted down by the interpolation kernel.

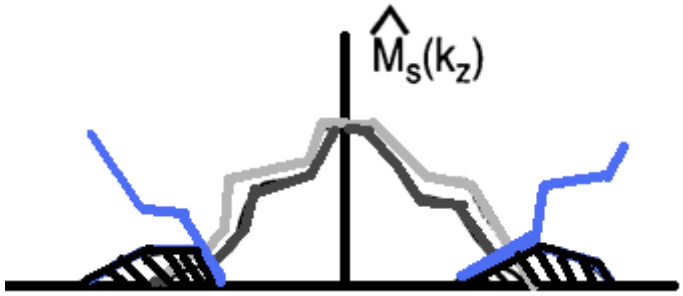

Figure 2-2b: The increase in the total area of hashed lines representing aliasing artifacts results from compounding of aliasing artifacts during each of multiple interpolation steps during image registration.

Figure 2-2: The interpolation process represented in the spectral domain. (**Adapted from reference [10].**)

Further, the interpolation process is more accurate in the in-plane direction. If the motion during a study is predictable, then we can change the slice orientation to restrict major component of the motion to in-plane direction. This will improve quality of motion correction by reducing through plane slice movement and interpolation related errors. As far as interpolation kernel is concerned, a truncated sinc interpolator was used for all the interpolation process.

2.1.3 Variable Slice Thickness

In fMRI studies with head motion, thinner and contiguous slices improve quality of image registration by increasing robustness to susceptibility artifacts and effects from its interactions with motion, increasing data sufficiency and by improving interpolation errors from inadequate sampling as described above. Use of thinner slices however, requires additional slices to cover the same volume of interest and increases scan time while lowering SNR. Both of these effects might not be desirable in fMRI studies.

The variable slice thickness acquisition scheme acquires images with thinner slices in the lower part of the brain near the sinuses where signal loss and dephasing artifacts are most prominent. Thus signal voids and intensity fluctuations from through plane dephasing are reduced in the lower brain regions. The superior parts of the brain which are relatively unaffected by susceptibility artifacts are sampled with thicker slices. With proper choice of the ratio of thick to thin slices, one might be able to improve temporal resolution by faster coverage of the upper brain regions via thicker slices, while still be able to recover some signal in the lower brain regions by using thinner slices.

All of the above approaches to optimize slice parameters in order to improve motion robustness of fMRI were investigated in phantom studies with positive results. Some of these interventions performed better than others in improving the robustness to motion in phantom studies. As such, a promising subset of these approaches - use of thinner slices as described in section 2.1.1 and use of variable slice thickness, section 2.1.3 were investigated in human subjects. The methods used for these studies are outlined in the subsequent sections along with the obtained results.

2.2 Slice Thickness

In addition to causing signal voids and artifacts in stationary images, intra-voxel dephasing is likely to be head orientation dependent as the underlying field inhomogeneity pattern changes with motion induced alteration of the susceptibility mismatch interfaces. Motion might increase signal loss or alter patterns of signal loss from one time point to another and cause intensity fluctuations thereby introducing errors and variance in the fMRI time series. Degradation of images in this manner might lead to incomplete registration and consequently, reduce the sensitivity of detection of functional contrast. Decreasing slice thickness reduces the field inhomogeneity related intra-voxel dephasing and signal voids and makes images more robust to artifacts from susceptibility and motion. As a result, the quality of images in the time series and the accuracy and completeness of motion correction might improve significantly by use of thinner slices in fMRI.

To ascertain our hypothesis, experiments demonstrating the benefits from use of thinner slices in fMRI were carried out in phantoms and human subjects.

Phantom Studies

METHODS: A spherical phantom with composition mimicking the electromagnetic environment in the human head was constructed and artificial structure and air spaces were introduced to emulate the susceptibility mis-matched interfaces present in the brain. As shown in **figure 2-3**, the phantom was made of gelatin-agar gel, T1=1100 ms, T2=80 ms [62] and contained artificial structures and airspaces to mimic tissue.

Figure 2-3: a. Axial **b.** Coronal **c.** Sagittal views of the phantom with spherical air space and incorporated structures to mimic the sinuses and brain morphology. These images were acquired using a T1 weighted sequence.

Using a customized, computer-controlled, MR compatible, motion platform capable of precise and repeatable automatic and controlled rotational and translational motion inside the scanner, the phantom was moved according to a pre-determined "saw-tooth" motion paradigm with rotations primarily in the coronal plane The paradigm was repeated across scans while ensuring consistency of external conditions across the different methods being investigated for mitigation of motion induced susceptibility

artifacts. The motion corrupted images in the time-series were then realigned to a reference image. The repeatability of the motion paradigm was characterized outside the scanner by performing several independent trials of the motion, (maximum angular displacement of $\pm$ 5 degrees), and measuring it with an external infrared motion tracking device (Optotrak® Infrared Tracking System, NDI products, Waterloo, CA). This tracking device measured motion of the phantom by using infra red reflections from markers attached to the phantom. The accuracy and reproducibility of the rotations of the phantom during independent runs were consistent to $\pm$ 0.02 degrees as shown in **figure 2-4**.

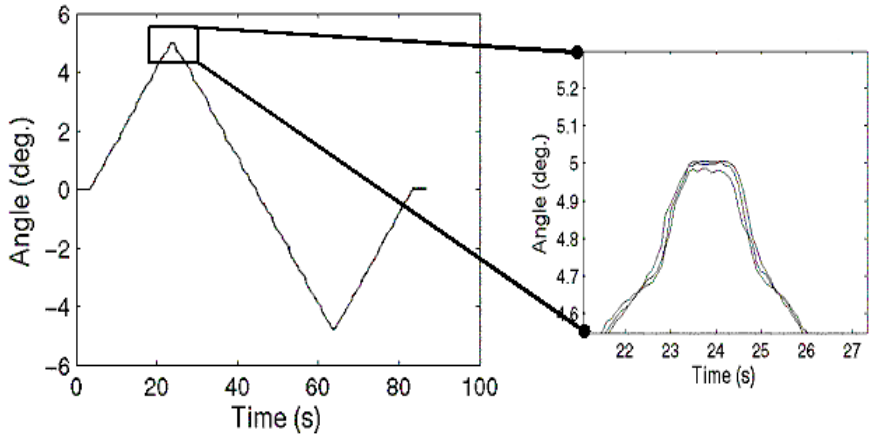

Figure 2-4: Three repetitions of a "saw-tooth" motion paradigm, max rotation $\pm$ 5.0 degrees, characterized by an external infrared tracking device. The zoomed image (inset right) shows the precision of the phantom motion paradigm to within $\pm$ 0.02 degrees across three repetitions.

The residual Normalized Root Mean Square Error (NRMSE) between reference image and the images in the time series were calculated for images with and without realignment. The reduction in residual NRMSE (e.g., considering zero NRMSE for "perfect" motion corrected time series) after realignment was expressed as a percent of

the NRMSE of the non-realigned case. This percent reduction in NRMSE was used as a metric to determine the effectiveness of the suggested methods and parameters.

Four independent repetitions of the phantom experiments were conducted. During each experiment, a 3T GE Signa scanner was used to acquire images of the phantom as it moved according to the previously described "saw-tooth" motion paradigm. The first few images in the time series were acquired without any motion and used as reference for registration of subsequent images in the time series. A Gradient Echo (GRE) sequence with TR=6 s, TE=27 ms, FOV 24 cm, data matrix [64 X 64] with flip Angle (FA) of 90 degrees and, an in-plane resolution (3.75 X 3.75 mm) was used during separate scans with contiguous slices of thickness ranging between 2 mm up to 6 mm with 1mm increments. Forward only and combined forward and reversed spiral acquisition trajectories were used for data acquisition and, the images were reconstructed with a standard CP gridding reconstruction method [40] using a static fieldmap and an iterative image reconstruction method that used a dynamic fieldmap. These reconstruction methods and their individual effects on motion correction will be discussed in detail in the next chapter. The MCFLIRT routine, part of the FSL software package (Oxford University, www.fmrib.ox.ac.uk/fsl) was used to register the images to a reference image chosen at the beginning of each run.

The ability of acquisition parameters – slice parameters in this case, to improve robustness of fMRI to motion were compared by quantifying the active voxels restored post motion correction (in time series with intentional motion present) compared to the same activation paradigm carried out without motion.

RESULTS: During four independent phantom trials, images were acquired with slices of thickness from 2 mm up to 6 mm with 1 mm increments using combined forward and reversed spiral acquisition while the phantom performed the motion paradigm described in **figure 2-4**. The decrease in percent NRMSE of the registered images at the two inflection points of the saw-tooth paradigm, corresponding to the position of largest displacement from the reference image, were averaged and compared across different slice thicknesses. A general trend of increased realignment accuracy or larger reduction in percent NRMSE was observed with thinner slices across all four phantom trials and across each reconstruction methods listed. As stated above, the reconstruction methods affect the accuracy of the motion correction. This effect will be investigated further in the next chapter. However, for purpose of study of slice thickness, each of these reconstruction methods can be analyzed independently of their individual effects on quality of motion correction. **Figure 2-5** shows the trend of greater motion correction accuracy with thinner slices is replicated across all the reconstruction methods.

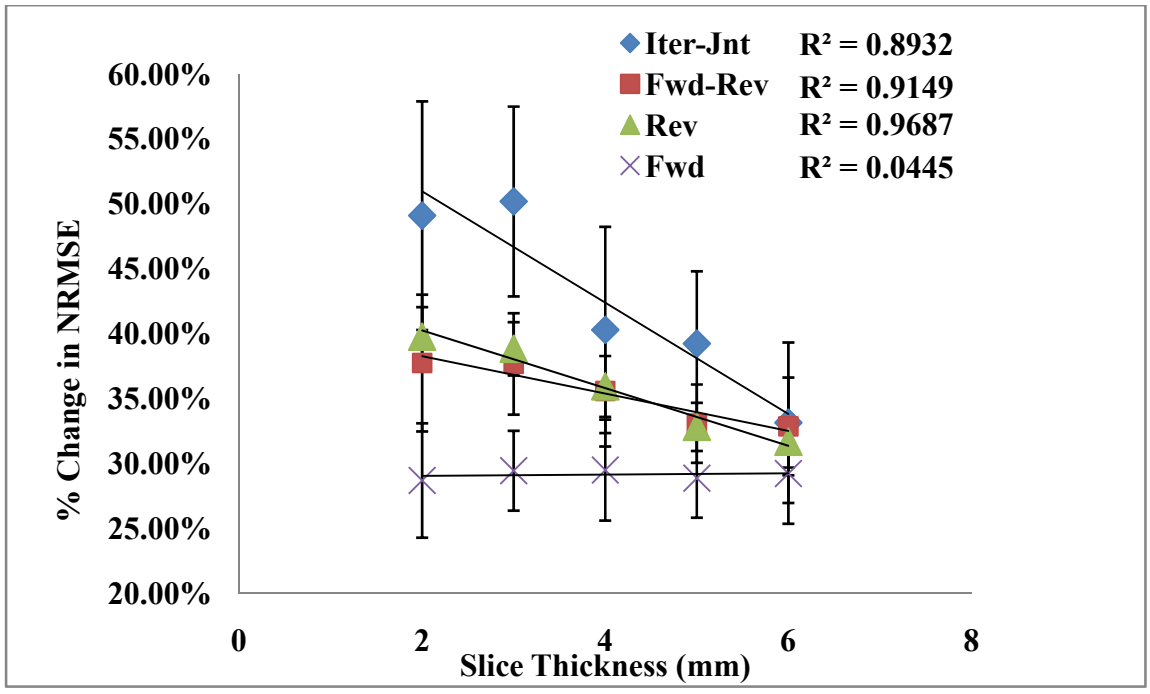

Figure 2-5: Comparison of the effects of slice thickness on motion correction.

Use of thinner slices leads to better quality of motion correction as evident from **figure 2-5**. A linear relationship was observed between thinner slices and improvement in motion correction for iterative reconstruction with dynamic fieldmaps (R^2=0.89), reversed spiral only acquisition (R^2 = 0.97) and combined forward and reversed spiral acquisitions (R^2=0.92). These results were consistent across all four experiments. The use of thinner slices with forward spiral only acquisition did not improve the quality of motion correction compared to thicker slices. This is because its vulnerability to in plane susceptibility gradients, quite possibly, has a much larger contribution to the image artifact across all slice thickness compared to signal loss from through plane spin dephasing.

Human Studies

METHODS: Two different studies were carried with human volunteers. For the first study, described below, the results obtained from the phantom experiments were validated in three human subjects. The subjects performed calibrated head motion only and were not presented with any functional stimulus. Using previously outlined percent reduction in NRMSE as a metric, improvements in quality of motion correction were characterized for experiments where images were acquired with different slice thickness – 3 mm vs. 5 mm vs. 8 mm, using different acquisition methods - forward only vs. reversed only vs. combined forward and reversed acquisition. These images were reconstructed using CP gridding reconstruction with static fieldmaps and an iterative reconstruction with dynamic fieldmaps.

The subjects were instructed to perform repeated and controlled "nodding" head motion inside the scanner. In order to guide their head movement, they were asked to follow a visual cue that consisted of a horizontal line (across the presentation screen) displacing vertically in a periodic and controlled fashion during the image acquisition process. To make the head movement consistent across acquisitions, a parallax-like alignment was set up with the described visual stimulus on screen and a fine plastic wire positioned approximately 10 cm from the subject, attached in the center of their visual-field in the scanner. The subjects were asked to maintain visual alignment of the wire and the visual cue by moving their heads. The motion of the head was controlled by varying the rate of vertical movement of the horizontal line on screen. This also ensured that the motion was restricted primarily in the through-plane direction (pitch) as transaxial slices were acquired.

Of the three subjects scanned, there was a significant variability in the consistency of head motion across acquisitions with differing slice thicknesses. While two of the three subjects were able to perform relatively consistent and repeatable motion as instructed, in case of the third subject, the head movement was widely variable across scans despite our best efforts. The motion profile of one of the more compliant subjects for independent scans with three different slice-thicknesses is included in **figure 2-6**. Images were acquired using a GRE sequence with TR=4 s, TE=27 ms, FOV 24 cm, data matrix [64 X 64] with in-plane resolution of (3.75 mm X 3.75 mm), FA = 90 degrees and, using slice thickness 3mm, 5mm & 8mm with forward spiral only and combined forward and reversed spiral acquisition trajectories.

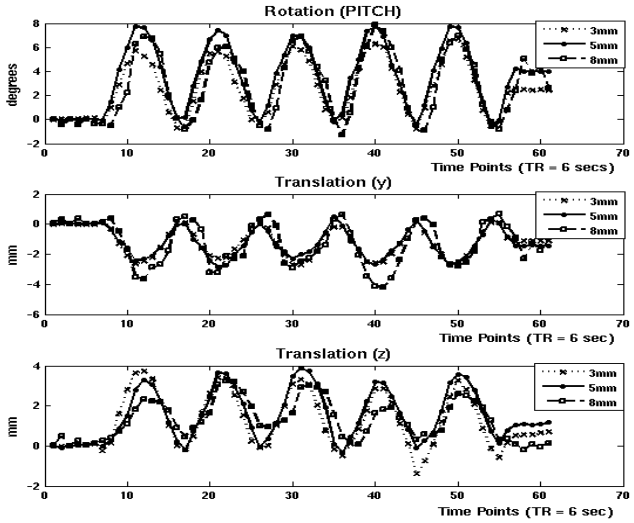

Figure 2-6: Motion profile of a compliant subject performing controlled head movement guided by a parallax arrangement. The profiles show rotation around x-axis or pitch of the head (top), translations in y (middle) & z directions (bottom) for three independent scans with slice thickness 3 mm, 5 mm, & 8 mm. Overall, the profiles are fairly consistent across acquisitions.

RESULTS: Despite the use of the previously described parallax guidance method, head motion was variable among subjects and, between scans for the same subject. Variability

in motion trajectories across independently repeated scans made is very difficult to do rigorous analysis of the effect of slice thickness on quality of motion correction as the extent and amount of error is appeared to be a function of motion. However, some general trends were observed across all trials. These trends are summarized and discussed qualitatively in the following paragraph.

As seen in **figure 2-7**, a combined analysis for all three trials showed that on average, reduction in NRMSE was higher for thinner slices, i.e. 3 mm and 5 mm slices performed better than 8 mm slice. Further, for one of the subjects, where the motion across scans was consistent across scans, (motion profile included in **figure 2-6**) a linear increase in quality of motion correction with thinner slices was observed (see **figure 2-8**).

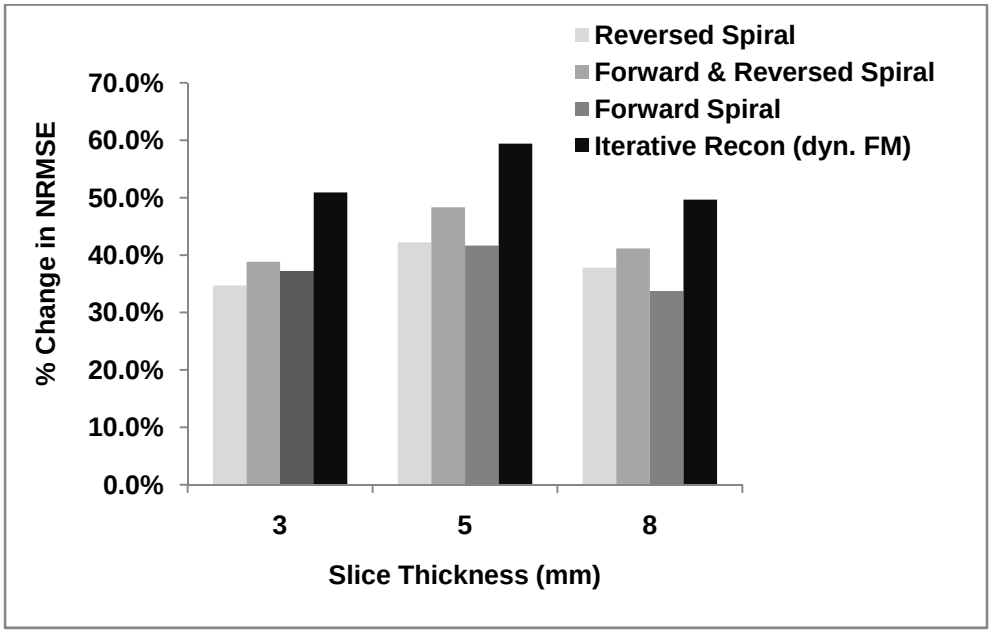

Figure 2-7: Although the 5mm slices performed better than 3mm slices, the 3mm and 5mm slices performed better than 8mm slice. The motion profiles through three trials are highly variable and might make comparison across slice thickness very difficult.

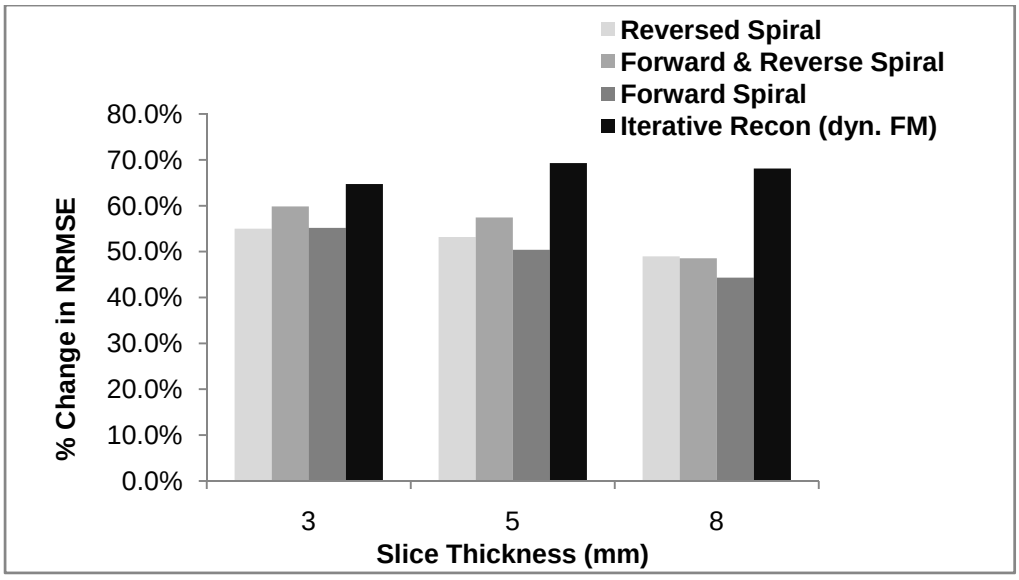

Figure 2-8: For one of the subjects where the motion profile was consistent across various scans, the trend of improved motion correction with thinner slices was observed. The motion profile for this subject has been included in figure 2.6.

The above results point to a possible variability introduced by motion trajectory. Thus, an effective comparison of the effect of slice thickness requires normalization of the effect of motion and is discussed later in the later section.

Functional Studies

METHODS: After evaluation of the effectiveness of the described acquisition parameters, acquisition methods and reconstruction methods in phantom and human subjects (no functional stimulus), in-vivo functional studies were carried out to investigate the impact of described methods on robustness of fMRI studies affected by head motion.

Initially, a few healthy volunteers were asked to perform a bilateral finger tapping task while being exposed to a visual stimulus. They were also instructed to perform controlled head movements during, task performance, using the previously described parallax arrangement. In most of the subjects, maintaining a parallax alignment with the

wire while performing the task elicited no coherent activation in response to the task. It was concluded that the subjects' attention was diverted from the actual functional task as they appeared to be more focused on maintaining a parallax arrangement and moving their head rather than performing the functional task. Thus the constraint of exact repeatability of the head movement across acquired time-series was reconsidered. The subjects were asked to rehearse the motion under supervision of the researcher prior to the scan and the subjects were instructed to keep the extent of head displacement as consistent as possible across scans to limit the range of motion. At any rate, this motion paradigm better approximated head motion one might expect during a real functional study. Each trial consisted of a visual stimulus - alternating checkerboard @ 8 Hz - while performing a motor - bilateral finger tapping - task. Individual trials consisted of 5 cycles of 20 s active task-performing (stimulus on) periods followed by 20 sec of control or rest period consisting of fixation at a cross in the center of a grey screen.

During each trial, six subjects were instructed to either **a)** hold their head still or **b)** performed calibrated movements according to instructions provided before the study. The rest and motion experiments were ordered randomly. For each subject, images were acquired using a GRE sequence with TR=2 s, TE=27 ms, FOV 24 cm, data matrix [64 X 64] with in-plane resolution of (3.75 mm X 3.75 mm) and, using slice thickness 3 mm, 6 mm & 9 mm with forward spiral only and combined forward and reverse spiral acquisition schemes. All human subjects were scanned with informed consent approved by the University of Michigan's Internal Review Board. A threshold of $Z \geq 4.0$ was set manually for all studies to detect active voxels.

RESULTS: To investigate the effect of slice thickness on functional studies, images at 3 mm/6 mm/9 mm slice thicknesses were acquired and the 3 mm slices subsequently averaged to produce VOI with identical in-plane and through-plane resolution for comparison with the 6 mm and 9 mm slices respectively. However, no coherent quantitative relationship between slice thickness and of detection of active voxels after motion correction was found. This might be due to the fact that unlike investigations of the effects of acquisition and reconstruction methods on motion correction, where raw k-space data is the same across various methods, investigation of effects of slice thickness was confounded by large variations in the motion parameters and consequent head orientation dependent susceptibility artifacts across scans with different slice thickness.

It was concluded that the effects of slice thickness on functional experiments need to be further investigated with more predictable and repeatable motion paradigms across acquisitions with different slice thickness. This is an area of active investigation at our facility and a device capable of reproducing repeatable motion of the head is under development.

2.3 Slice Profile, Spacing and Orientation

As already discussed earlier, sampling the object with thinner and contiguous slices increase the sampling frequency of the spatial spectrum of the object in the through plane direction and, reduces the aliasing energy contributed to the image spectra compared to sampling the object with thicker slices or slices with gaps respectively. Further, slice profiles with narrow spectral width reduce the amount of aliasing artifacts

and its propagation during various interpolation steps performed as part of motion registration process. The in-plane dimensions in 2D planar imaging are adequately sampled from a spectral perspective compared to the slice select direction is inherently undersampled. If significant motion occurs in the slice-select direction, the ability of registration algorithms is limited in properly correcting for motion. Completeness of motion correction can be enhanced by limiting motion to in-plane only or alternatively, if patterns of motion can be anticipated, then, gains can be made by prescribing the slices so as to limit the head motion in-plane. In all of the above studies, a shortened sinc interpolator of the FSL package (Oxford University, www.fmrib.ox.ac.uk/fsl) was used as it is the best convolution interpolator provided by the currently existing motion correction packages available to the fMRI community.

Phantom Studies

The phantom was imaged in all orientations, axial, sagittal, coronal with identical parameters and while performing the same motion. The motion was in the slice-select direction for axial and "through imaging plane" for sagittal direction but, "in imaging plane" for coronal prescription. A comparison of change in NRMSE pre vs. post motion correction in images where motion occurred in-plane (coronal acquisition) versus through plane (axial acquisitions) revealed that motion correction improved for in-plane acquisitions. Although a viable option, it is hard to predict the direction of motion in most fMRI studies, as such, despite its promise, this method was not explored in human studies. However, in special circumstances where the motion pattern is predictable and consistent across subjects, this method remains a viable option for improved performance of motion compensation step.

We compared a rectangular slice profile (RF spectrum is a "Sinc") with extended spectrum to a Gaussian slice profile (RF spectrum is "Gaussian"). The result of effect of slice profile on quality of motion correction is included in **figure 2-9**.

A constant VOI in the moving phantom was imaged with varying slice thickness/overlap: 3mm with 2mm gaps, 4mm slices with 1mm gap, 5mm slices with no gap. The slice-select gradient was then appropriately scaled to acquire 5mm slices (prescribed) but the actual slice thickness being 6mm (or 5mm slice with 1mm overlap), 7mm (or 5mm slice with 2mm overlap), & 8mm (or 5mm slice with 3mm overlap) respectively. This effectively correspond to 10%, 20% and 30% overlap as a fraction of the actual slice thickness with 5 mm center to center slice spacing and further improves sampling in through plane direction, thereby reducing aliasing artifacts.

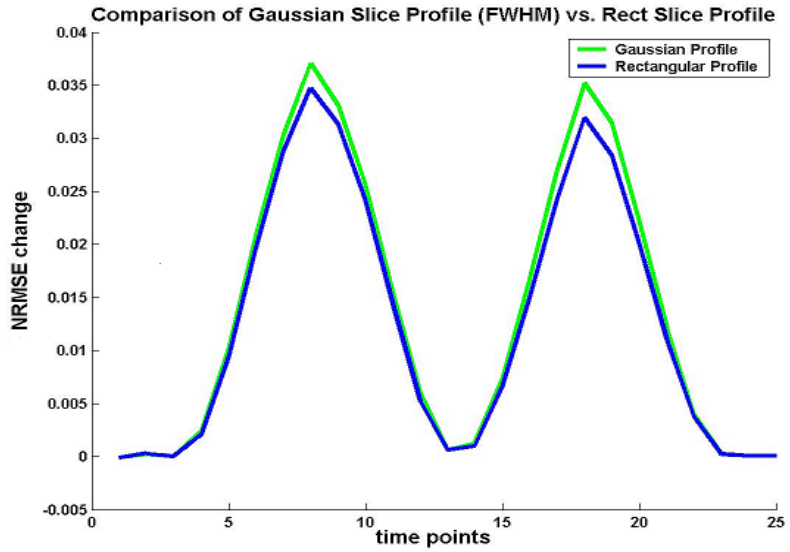

Figure 2-9: Although the use of Gaussian slice profile does seem to improve motion correction, the improvement, however, is very small.

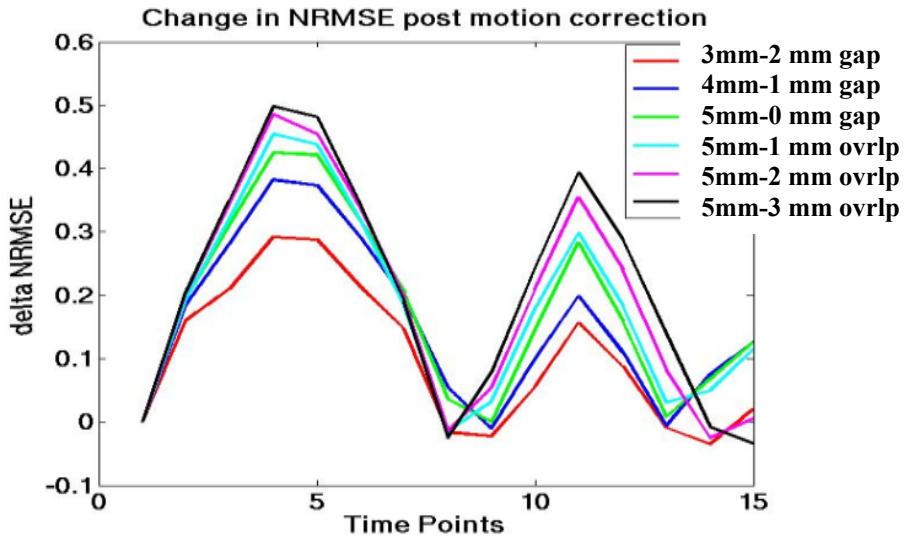

Figure 2-10: On reducing inter-slice gap from 2 to 0 mm, resulted in improved NRMSE reduction i.e., ~27% (2mm gap) to 41% reduction for no gap after motion correction. Using overlapping slice further improved the quality of motion correction, ~45%, ~48% and ~51% reduction in NRMSE for 10%, 20%, 30% overlap respectively.

Our investigations on optimizing slice profile, spacing and orientation yielded improvements in quality and completeness of the motion correction step. Further, though the overlapping slices improve quality and completeness of motion correction, they also might suffer from T_1 saturated effects as the overlap regions will be excited multiple times during a single scan. Overlap of slices might lead to an increase in susceptibility induced signal loss as the slices acquired are effectively thicker. In general, the benefits from these approaches were not compelling enough to explore their effects in functional experiments.

2.4 Variable Slice Thickness

Despite significant benefits from use of thinner slices in fMRI studies, associated temporal penalty and SNR loss often prevent investigators from using them in functional studies. The trade-off between signal recovery, image robustness and the listed disadvantages should be carefully considered. Our investigation in this area lead to the development of a variable-slice-thickness sampling scheme that uses thinner slices in lower brain regions, around sinuses, while the upper brain regions are sampled with thicker slices. Using such a method, we were able to improve the signal recovery in the lower regions where the susceptibility artifacts are most prominent while still maintaining a viable temporal resolution for functional studies.

A representative volume coverage scheme for a spherical phantom is shown in **figure 2-11**. Axial slices were excited in a spherical phantom with a uniform as well as variable slice thickness sampling scheme. However, the images were acquired in the sagittal plane so that profiles of the excited slices were observed. The top figure, (red) shows the sagittal (Y-plane slice) profiles of variable sampling with 2mm (thin) & 4mm (thick) slices & (bottom, blue) shows sagittal (Y-plane slice) profiles of uniform thickness of 3 mm. The VOIs are identical in both the figures but in case (top) of variable sampling, a third of the volume is covered by 2mm slices and the rest, by 4mm slices. This leads to an effectively similar TR for both the acquisitions. Other combination schemes can be explored dependent on the desired quality of images.

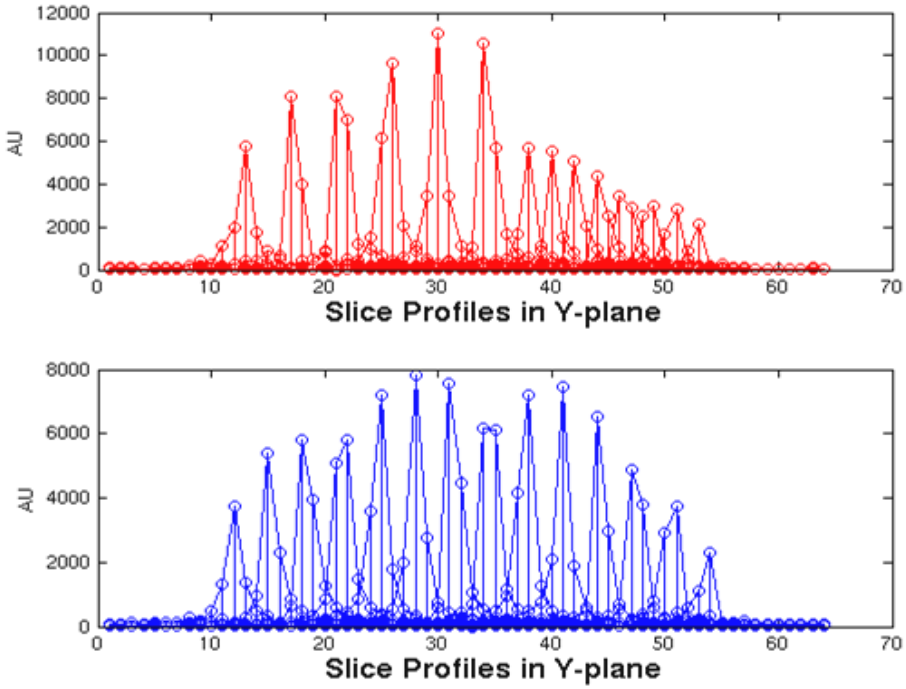

Figure 2-11: slice profiles for a variable (top) and uniform (bottom) sampling scheme for a spherical phantom

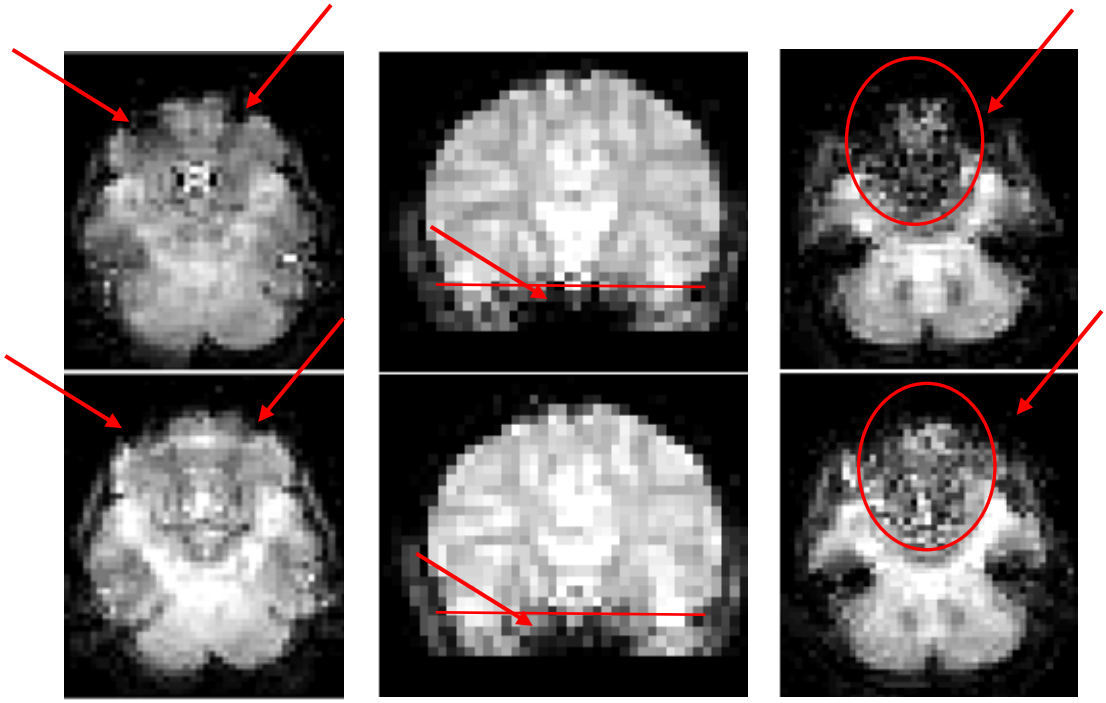

Figure 2-12: comparison of signal in the region around Inferior Frontal Cortex for uniformly thick 3 mm slices (top) and same region sampled with variable slice thickness 4mm/2mm sampling scheme (bottom).

Top row shows representative brain images (in region marked by the horizontal red line) acquired with uniform 3mm thick slices while bottom row shows same region sampled with variable slices, top two-thirds with 4 mm and bottom third with 2 mm slices. In the coronal section (center), the arrows emphasize the regions where the signal loss in top row is much greater than the bottom row coronal image acquired with thinner slices & averaged. In the two representative axial slices, the regions of larger signal voids are highlighted in the top figures compared to similar regions in the bottom row.

As is shown, use of variable slice thickness is able to recover the signal in the lower brain regions while maintaining the temporal resolution of the fMRI studies. Although the idea of using variable slice thickness can be extended to functional studies with significant benefit, some issues that might need to be considered are motion correction and SNR issues.

Motion Correction: Thinner slices have lower signal to noise ratio (SNR) compared to the thicker slices. This creates a very real possibility that the currently used image realignment algorithms that penalize intensity based dis-similarity between images, might be stuck in artificial local minima thereby increasing the chances of failure of the realignment algorithm to properly register images. In order to circumvent this possibility, algorithms that use similarity measure that are relatively robust to these kinds of intensity discrepancy should be used; for example, Mutual Information (MI) based objective function might be more appropriate. Another solution might be to acquire a high resolution anatomical image at the beginning of the scan and use it as a reference to realign individual slices or entire volumes to this reference image in a manner similar to

one used by Kim et. al. [49]. Further work needs to be done in this area to determine the optimal motion correction strategy in this scenario.

SNR and its impact on activation detection: The SNR for the images acquired with thicker and thinner slices might be different. As such, one needs to further investigate methods for comparing the statistical power of the "active" voxels when using variable slice thickness.

2.5 Discussions and Conclusions

Merboldt et al, [53] have shown that the use of thinner slices for imaging of the lower parts of the brain in stationary subjects reduce susceptibility induced signal loss near the sinuses and make functional studies possible in these regions. In presence of head motion, use of thinner slices becomes even more relevant. Besides preventing signal loss in the lower brain regions and restricting the impact of dynamic interactions between head motion and susceptibility artifacts, thinner slices improve image fidelity and increase data sufficiency in through plane direction, consequently, reduce interpolation artifacts.

Our investigations showed that thinner slices resulted in better motion correction in phantom experiments where the motion across various scans was repeatable. In human experiments, when the motion across scans with different slice thicknesses was fairly repeatable, thinner slices improved quality of motion correction and, in general thinner slices, (both 5 mm & 3 mm) performed better than 8mm slices. These results indicate that thinner slices are advantageous from a motion correction standpoint; however, their

effects on functional studies need to be further investigated by incorporating ways to normalize or remove the effects of variability in motion parameters across independent scans with different slice thickness.

Reducing slice thickness has its disadvantages - reduction in SNR and temporal resolution - undesirable effects in many functional imaging studies. Despite these negatives, in regions of high signal loss from spin dephasing or, at tissue/air interfaces where dynamic changes in head orientation can have a debilitating effect on the fMRI studies, robustness availed by thinner slices in terms of image quality, increased BOLD sensitivity and subsequently, quality and completeness of motion correction might outweigh SNR issues.

Use of variable slice thickness utilizes the benefits of thin slices while maintaining sufficient temporal resolution to enable its use during fMRI experiments. However, some issues surrounding motion correction and activation detection issues need to be further investigated before it can be used as a viable method in functional studies.

CHAPTER 3

Acquisition and Reconstruction Methods

3.1 Background and Theory

3.1.1 Acquisition Trajectories

Rapid image acquisition methods such as spiral and EPI have made functional MR imaging possible by freezing head and physiological movements and increasing temporal resolution. Unfortunately, these techniques are extremely sensitive to field inhomogeneity effects. In presence of in-plane field gradients especially near tissue-air interfaces, images acquired with forward spiral acquisition is vulnerable to signal dropouts and image distortions from shifting and skewing of the acquisition k-space trajectory in a manner briefly summarized below [54, 63].

In presence of field inhomogeneity, $\Delta B_0(x)$, the MR signal, **s(t)** at a spatial location **x** and, in presence of encoding gradients **G(t)** is:

$$\mathbf{(3.1)} \quad s(t) = \int m(\mathbf{x}) e^{-i2\pi k(t).\mathbf{x}} e^{-i\Delta B_o(x)(t+TE)} d\mathbf{x}; \qquad \mathbf{x} = [x, y]^T$$

The desired or ideal k-space trajectory is the time integral of the encoding gradients and represented as:

$$\mathbf{(3.2)} \quad k(t) = \left[k_x(t)\ k_y(t)\right] = \frac{\gamma}{2\pi}\int_0^t G(t)dt$$

Due to contributions from the field inhomogeneity $\Delta B_0(x)$, there exists an additional in-plane susceptibility gradient that is added to the encoding gradients. This additional in-place gradient can be characterized by Taylor series expansion of $\Delta B_0(x)$ and, incorporating the first two terms into the signal equation **3.1**. The net effect of these components of the field inhomogeneity is shown in equation **3.4**:

(3.3) $$\Delta B_0(x) = \Delta B_0(x_0) + \gamma G_B(x_0).(x - x_0) + \ldots..$$

(3.4) $$s(t) = e^{-i(\Delta B_0(x_0) - \gamma G_B(x_0).x_0(t+TE)} \int m(x) e^{-i2\pi(k(t)+k_B(t+TE).x} dx;$$

In presence of inhomogeneity, $\Delta B_0(x)$, the actual encoded trajectory of the "modified" signal equation, has two additional terms compared to the ideal k-space trajectory. These additional components are listed in equations **3.5** & **3.6**.

(3.5) $$K_{total}(t) = k(t) + k_B(t + TE).$$

(3.6) $$k_B(t) = \frac{\gamma}{2\pi} G_B t; \quad k_B(TE) = \frac{\gamma}{2\pi} G_B TE;$$

The first term in equation **3.6** causes the skewing of the k-space trajectory while, the second term causes the shifting of the k-space trajectory. The effect of the in-plane gradient on the acquisition trajectory is shown in **figure 3-1. Figure 3-1a** shows an ideal spiral trajectory, the **figure 3-1b** shows the shifted and skewed forward spiral trajectory in presence of 0.009g/cm in the **x** direction. In GRE fMRI imaging, this shifting and skewing of the k-space trajectory lead to signal loss and degradation of the image as the center 'DC' region of the k-space is not adequately sampled.

Shorter TE might mitigate some of these effects by reducing the total shifting (see **figure 3-1c**) away of the sampled k-space trajectory from the actual k-space, in BOLD

fMRI, reduction in TE might reduce the BOLD sensitivity. Another solution to this problem is to use reversed spiral acquisition trajectory. Using a reversed spiral method, the signal in the affected area can be recovered to a large extent. This is because, in reversed spiral trajectory, the effect of the skew component is the reverse i.e., k-space trajectory is skewed towards the k-space center leading to a better coverage of the central region of k-pace (see **figure 3-1d).** The associated loss of T2* sensitivity due to shortened effective TE for the reversed spiral method is offset by improved recovery of signal in regions affected by signal loss or distortion artifacts.

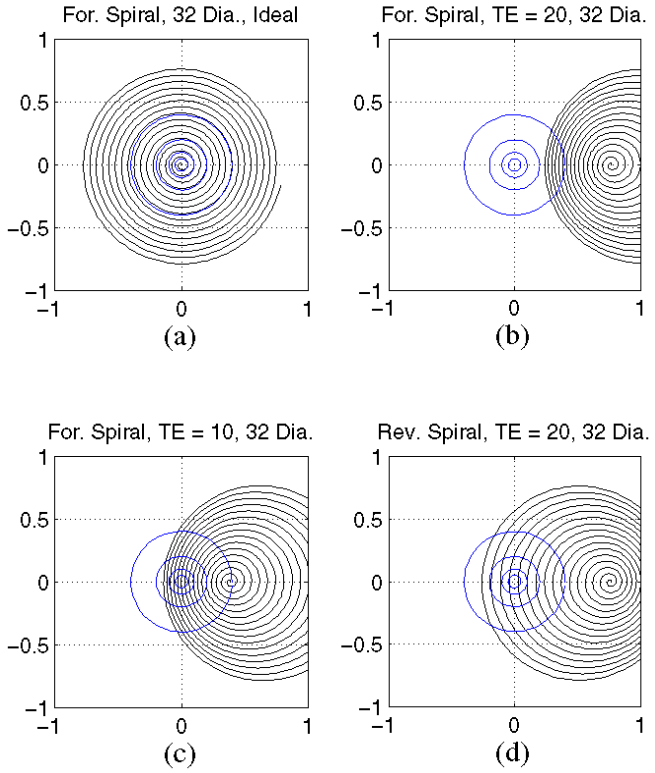

Figure 3-1: Demonstration of k-space coverage for different acquisition parameters for a local gradient of 0.009 g/cm. (a) The ideal acquisition trajectory, (b) gradient echo, forward spiral with TE = 20ms, (c) forward spiral, TE = 10ms, (d) reverse spiral, TE = 20ms.

A combination of forward and reversed spiral acquisition increases SNR of images without any temporal penalty and improves activation detection despite in plane gradients [54, 63-65]. Thus combined forward & reversed spiral acquisition can be used to improve the accuracy of realignment by increasing SNR and reducing image corruption due to motion induce susceptibility artifacts. Improved image registration and increased robustness to secondary artifacts will reduce variability in fMRI data and increase the sensitivity of detection of functionally active regions.

3.1.2 Iterative Image Reconstruction

In spiral imaging, susceptibility induced macroscopic field inhomogeneity causes significant image degradation via blurring and image distortions [66]. When reconstructing images using Conjugate Phase (CP) gridding methods [40], off-resonance effects from field inhomogeneity are corrected by using a B_0 field inhomogeneity map acquired at the beginning of the time series – static fieldmap. Static fieldmap will not correct for dynamic changes in the B_0 inhomogeneity mostly due to head motion during subsequent time points. Further, the assumption of smoothly varying fieldmap made by CP reconstruction methods is not necessarily accurate at the tissue/air interfaces. These factors limit the ability of CP reconstruction method to correct for B_0 inhomogeneity effects, especially, when these effects change dynamically. On the other hand, model based iterative image reconstruction may better approximate MR imaging process in presence of field inhomogeneities [55].

The iterative image reconstruction problem can be stated as an estimation of the object, $\mathbf{m(x)}$ from the measurements, $\mathbf{g} = (g_1,..., g_N)$, which are noisy samples of the signal, $s(t)$: $g_i = s(t_i) + \varepsilon(t_i)$, for $i = 1,\ldots,N$. A detailed description of this reconstruction is

included in [55]. Assuming finite sampling of the continuous object, an estimate of the object can be given by:

(3.7) $$\boldsymbol{m}(\mathbf{x}) = \sum_{j=1}^{M} \boldsymbol{m_j b}(\boldsymbol{x} - \mathbf{x}_j);$$

where $\mathbf{x}_j$ denotes the coordinates of the j^{th} voxel, and $\mathbf{m_j}$ denotes the unknown basis expansion coefficient of the j^{th} voxel, and **b(x)** is a pixel indicator function, typically a 2D "rect" function. The reconstruction problem is to estimate $\mathbf{m} = (m_1,..., m_M)$ from **g**. Substituting equation **3.7** into the signal equation and simplifying yields:

(3.8) $$\boldsymbol{g} = \boldsymbol{Am} + \boldsymbol{\varepsilon},$$

Here, **ε** is a noise vector (including model error), and **A** is a N×M system matrix with entries:

(3.9) $$\boldsymbol{a_{ij}} = \boldsymbol{e^{-i2\pi k(t_i).x_j} e^{-\Delta w(x_j)t_i} B}(\mathbf{k}(\boldsymbol{t_i}));$$

***B*(k)** denotes the 2D FT of ***b*(x)**. Each $\boldsymbol{a_{ij}}$ represents the contribution of the j^{th} voxel to the i^{th} signal sample. Given this formulation, object vector **m** can be estimated from the measurement vector **g** directly from the model (**g** = **Am**+**ε**) by finding the least-squares fit to the measurements:

(3.10) $$\tilde{\boldsymbol{m}} = \mathbf{min_m} \|\boldsymbol{g} - \boldsymbol{Am}\| = (\boldsymbol{A'A})^{-1}\boldsymbol{A'g}$$

An iterative minimization using conjugate gradient (CG) algorithm is used for the estimation of the image **m**.

3.1.3 Joint image and fieldmap calculation – dynamic fieldmap estimation

Use of iterative reconstruction method provides a suitable framework for the joint estimation and use of dynamically updated fieldmaps during reconstruction of images at each time point using forward and reverse spiral data. To summarize briefly, the joint fieldmap and image estimation process starts by considering both the image and the fieldmap at any given time point as unknown quantities. Starting with an initial estimate of the fieldmap that is held fixed, (for this step, fieldmap was initialized to static fieldmap calculated at the beginning of the scan), the image is estimated iteratively using a CG algorithm as described in the previous section. Then, keeping the estimated image at the current step fixed, the fieldmap is estimated or updated using an iterative gradient descent algorithm. This step of alternating between image and fieldmap estimation is continued until sufficiently accurate estimates of both, the image and fieldmap is obtained at each time point. The details of this procedure are elaborated in the work of Sutton et. al. [55, 56].

The dynamically updated fieldmaps are better able to capture and correct for temporally changing spatial off resonance patterns due to interactions between movement and head orientation dependent B_0 inhomogeneity effects compared to the static fieldmap. Thus, use of iterative reconstruction with jointly estimated and dynamically updated fieldmaps may be more beneficial method of image reconstruction in presence of head motion. This method might not only produce better quality images but alsof improve motion correction by reducing variance in the fMRI dataset via mitigation of motion induced susceptibility artifacts.

3.2 Static versus dynamic fieldmaps: A Study

One of the most prominent detrimental effects of secondary artifacts in fMRI comes from interaction between susceptibility artifacts and motion. Motion reorients the interface between air cavities and brain tissue both of which have different susceptibilities. This can cause dynamic variations in off-resonance patterns throughout the brain and, as a result, dynamically changing artifacts. To emphasize this point, Simulation studies have been undertaken by Andersson et. al. [7], and Truong et. al. [67]. Image artifacts from dynamically changing head orientation dependent sources reduce the accuracy of image registration in ways that have been described previously.

In this section, we characterized the position dependent off-resonance artifacts in a susceptibility phantom and human subjects and investigated the effectiveness of image reconstruction methods for spiral fMRI that do off-resonance correction using different types of fieldmaps. In particular, we evaluated Conjugate Phase (CP) gridding reconstruction with - static and motion corrected fieldmaps [40]; and a model based iterative image reconstruction with - static, motion corrected, and jointly estimated dynamic fieldmaps [55, 56].

Phantom Studies

METHODS: A small metal pin was attached to the inferior surface of a spherical silicon phantom to emulate the field distortions in the human head. Axial images were acquired using a 3T GE scanner with, TE=25msec, TR=5s, FOV=22cm, size [64x64] and a combined reverse & forward spiral GRE sequence. The phantom was imaged at four orientations. Between each orientation, the phantom was rotated by 4 degrees in the coronal plane and a translated by 1mm in the z-direction. Four shot, high resolution

images and fieldmaps, size [256 x 256] were acquired at each location and motion parameters were estimated with FLIRT using these images.

Fieldmaps were calculated using four methods,

1) "**measured"** –separate fieldmaps were obtained at each of the four locations/orientations of phantom. At each orientation, two images were acquired with slight differences in their echo times and the phase accumulated during ΔTE was used to calculate the fieldmaps. Fieldmaps estimated in this manner represent the best possible estimate of the underlying off-resonance pattern at different orientations of the head.

2) "**static"** –fieldmap at first position was measured in a manner described in the measured fieldmap section. This fieldmap was then used for all subsequent positions, (currently used in most fMRI studies).

3) "**motion corrected"** –estimated motion parameters were used to rotate and translate the static fieldmap to the current orientation of the phantom.

4) "**dynamically estimated"** –joint image and fieldmap estimation method was used to obtain dynamically updated fieldmaps. We compared the images reconstructed using CP reconstruction method and iterative reconstruction method using - static, rotated, ideal and dynamic fieldmaps.

Dynamically estimated fieldmaps were used with the iterative reconstruction only. The reconstructed images at the four positions were registered to the initial position, using MCFLIRT of the FSL motion correction package, and the Normalized Root Mean

Square Error (NRMSE) of the motion corrected images and reference image (image position 1) was compared across the various image reconstruction and fieldmap estimation methods.

RESULTS: The first row in **figure 3-2** shows the off-resonance patterns or fieldmaps (FM) at four different orientations of the phantom. These patterns differ significantly with changing phantom orientation. Image artifacts due to changing off-resonance patterns are most prominent at position 4 for images in second row (static FM) and third row (motion corrected FM). At this position, the phantom is "furthest" from its original orientation and, as can be seen in the first row and the off-resonance patterns differ maximally from original pattern. Note, images in the fourth row (dynamic FM) and fifth row (measured FM), the artifacts in images at position 4 are suppressed as the dynamically updated and measured FMs capture the "changed" off-resonance patterns more accurately than static and motion corrected FM at this orientation. In general, the effectiveness of static FM based correction, as included in the second row is reduced as the phantom orientation moves further from its original position.

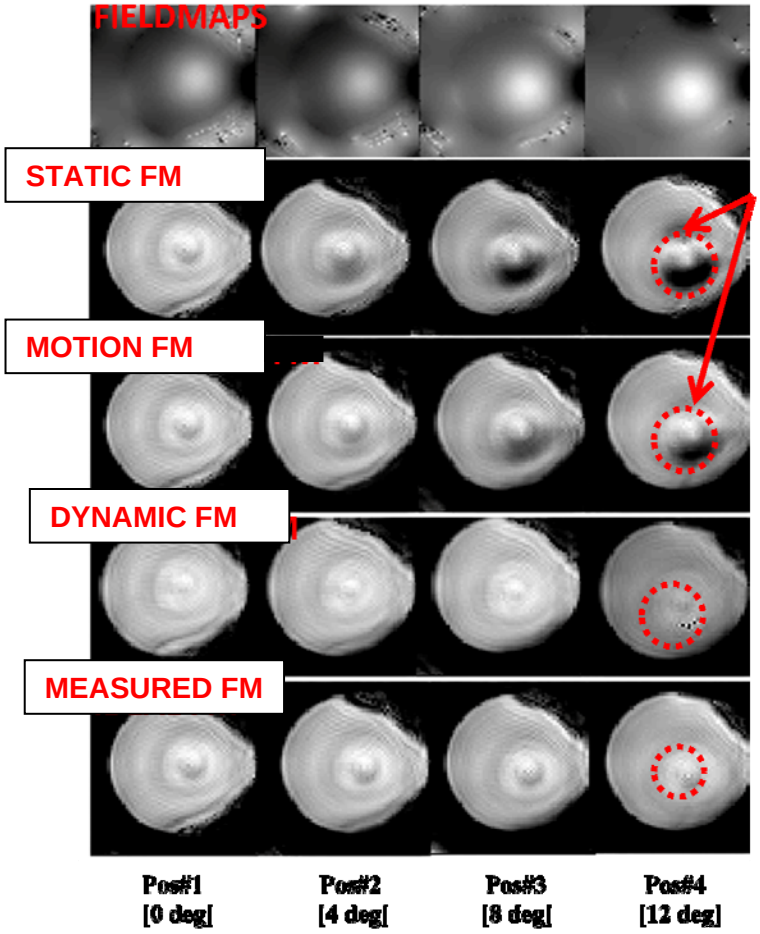

Figure 3-2: The top or **first** row shows the measured fieldmaps calculated at four different positions of the phantom. The **second** row shows the images reconstructed with the static fieldmaps at the four positions. The **third** row shows images reconstructed with motion corrected fieldmaps, the **fourth** row shows the jointly estimated and dynamically updated fieldmaps and the **fifth** row shows images reconstructed with directly measured fieldmaps at each orientation.

Motion Correction: **Table 3-1** summarizes the effect of the above listed off-resonance correction methods on the quality of image registration. CP gridding and iteratively reconstructed images of the phantom at position #4 were registered to the images at position #1, (reference) and the NRMSE between registered and reference was used as a measure of effectiveness of motion correction, lower NRMSE suggesting a more accurate registration. For measured and dynamically updated FM, the NRMSE is the lowest and

equal to each other suggesting that these methods more effectively reduced dynamic off-resonance artifacts and improved image registration. As expected, static FM corrected image perform worse both in iterative and CP case followed by images reconstructed motion corrected fieldmaps while measured & dynamically estimated FM performed the best.

Table 3-1: A comparison of the error after motion correction between the reference and the image displaced to the furthest (fourth) position of the phantom.

NRMSE	STATIC	MOT. COR	DYN	MEASURED
CP	**23%**	**22%**		**20%**
ITER	**21%**	**20%**	**16%**	**16%**

Human Studies

METHODS: A volunteer was instructed to place their heads in three different positions. Position #1 - control (reference) position, Position #2 - movement in through plane only (Pitch), Position #3 - both in-plane rotation and through plane movement. Axial images were acquired much the same way as in the phantom studies described above, with four different fieldmaps: static, motion corrected, dynamic and measured. Four-shot, high resolution images and fieldmaps, size [256 x 256] were acquired at each location and motion parameters were estimated with FLIRT using these images for motion correction of fieldmaps.

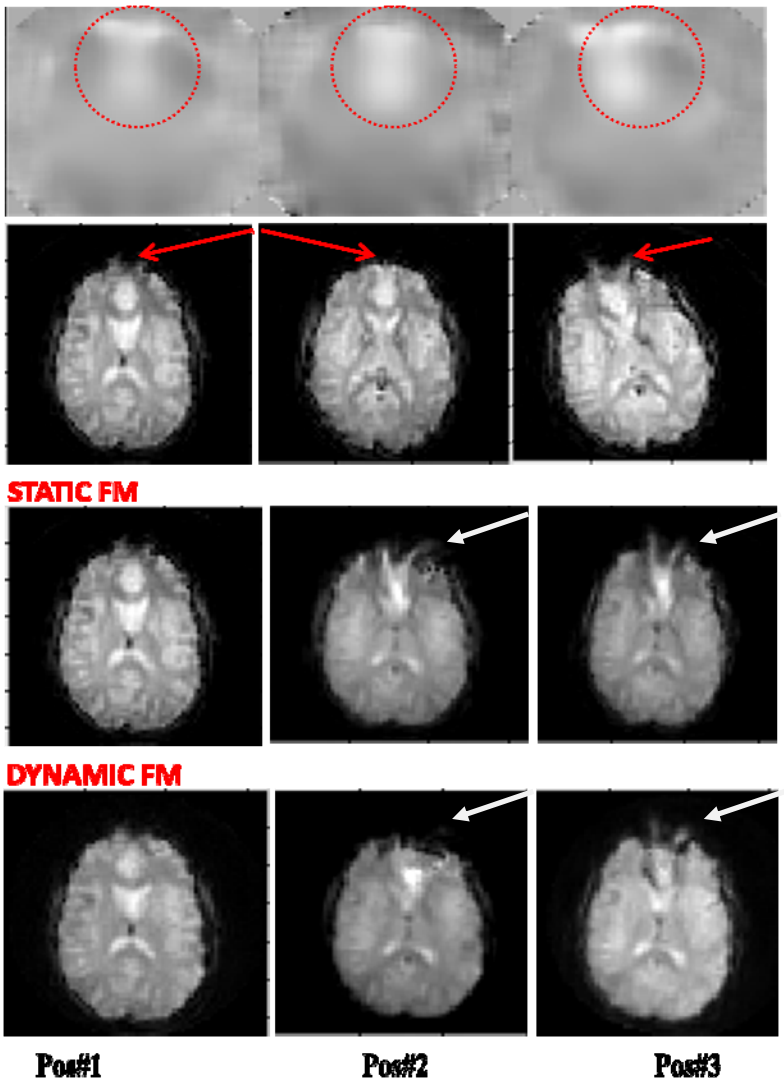

Figure 3-3: The top row shows the fieldmaps calculated at each orientation of the head, pos#1 is the reference, pos#2 has a through plane displacement and pos#3 has rotation and through plane displacement. The second row shows images reconstructed with measured fieldmaps. The static fieldmap reconstructed images at position 2 & 3 show a large distortion (arrows) near the sinuses. The jointly estimated dynamic fieldmap is better able to mitigate these distortions and leads to reconstructed images that are comparable to the images with true fieldmaps.

RESULTS: We found that iterative reconstruction with dynamically updated fieldmaps was best able to compensate for orientation dependent dynamic off-resonance artifacts. The commonly used static fieldmap based off-resonance correction was least effective.

This trend was also reflected in the effectiveness of motion correction of images reconstructed using the above listed methods and off-resonance correction measures.

3.3 Acquisition Methods & Reconstruction Methods: An Experimental Study

Phantom Studies

METHODS: A spherical phantom with composition and shape mimicking the human head was constructed and moved according to a saw-tooth motion paradigm, described previously (for details, see **section 2.2**), with a computer controlled motion platform. The paradigm was repeated across scans while ensuring consistency of external conditions across the different methods being investigated. The residual Normalized Root Mean Square Error (NRMSE) between reference image and the images in the time series were calculated for images with and without realignment. The reduction in residual NRMSE (e.g., considering zero NRMSE for "perfect" motion corrected time series) after realignment was expressed as a percent of the NRMSE of the non-realigned case. This percent reduction in NRMSE was used as a metric to determine the effectiveness of the suggested methods and parameters.

Four independent repetitions of the phantom experiments were conducted. A Gradient Echo (GRE) sequence with TR=6 s, TE=27 ms, FOV 24 cm, data matrix [64 X 64] with an in-plane resolution (3.75 X 3.75 mm) was used during scans. Forward only and combined forward and reversed spiral acquisition trajectories were used for data acquisition. Images were reconstructed using a CP image reconstruction with static

fieldmaps and, with iterative image reconstruction method that used joint image-fieldmap estimation method to calculate dynamic fieldmaps at every time point.

RESULTS: **Figure 3-4**, compares improvements from using different acquisition and reconstruction methods in phantom experiments. Note: Previously, the same figure, (**Figure 2-5**) was used to analyze the effect of slice thickness on motion correction, however, the effect of reconstruction methods was not elaborated on. Iterative reconstruction with jointly estimated and dynamically updated fieldmaps consistently performed better than CP gridding image reconstruction using a static fieldmap across all slice thickness. Both image reconstruction methods, iterative reconstruction and the CP gridding reconstruction, used the same data from combined forward and reversed spiral trajectory. Among the static fieldmap methods, percent reduction in NRMSE with reversed spiral acquisition and combined forward and reversed acquisitions were consistently higher than forward spiral acquisition across all slice thickness.

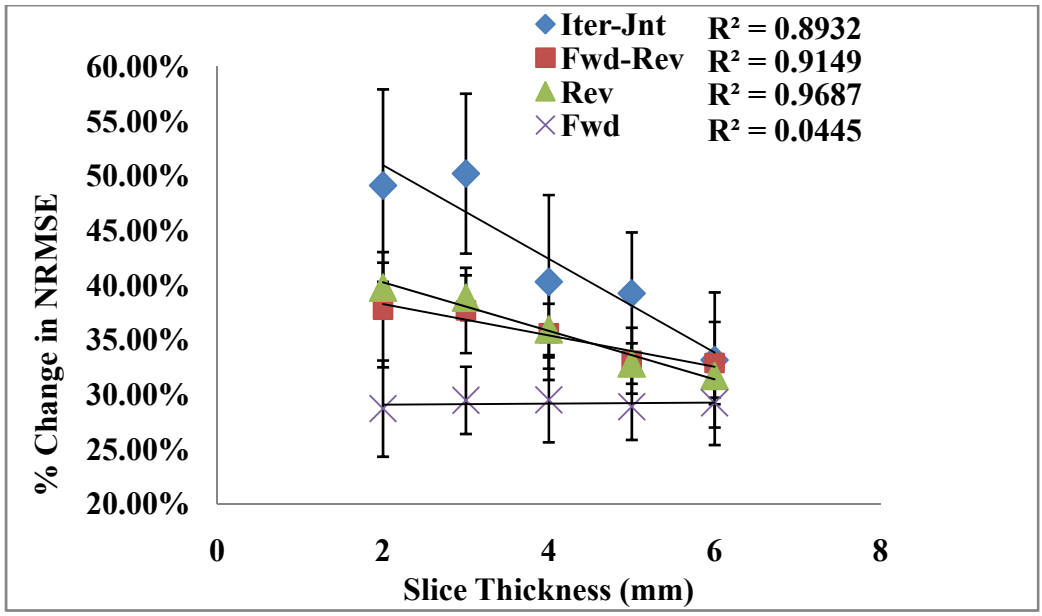

Figure 3-4: During four phantom trials, quality of motion correction for images reconstructed with model based iterative reconstruction method with dynamically updated fieldmaps (Iter-jnt) were far was better than all of the CP gridding methods with static fieldmaps. Combined forward & reverse spiral (Fwd-Rev) acquisition and reversed spiral (Rev) acquisitions outperformed forward spiral (Fwd) only acquisitions.

Human Studies

METHODS: First, the subjects performed calibrated head motion without any functional stimulus. Using previously outlined percent reduction in NRMSE as a metric, improvements in quality of motion correction were characterized using different acquisition methods - forward only vs. reversed only vs. combined forward and reversed acquisition. Image reconstruction methods included CP image reconstruction with static fieldmap and iterative reconstruction with jointly estimated and dynamically updated fieldmaps. The subjects were instructed to perform repeated and controlled "nodding" head motion inside the scanner using a parallax-like alignment described in section 2.2.

Motion was restricted primarily in the through-plane direction (pitch) as transaxial slices were acquired.

RESULTS: For a representative 5 mm dataset (see **figure 3-5**), combined forward and reverse spiral acquisition was more robust to motion than reverse only and forward only acquisitions as measured by previously described NRMSE criterion. Use of iterative reconstruction method with jointly estimated and dynamically updated fieldmap resulted in the best quality of images and motion correction.

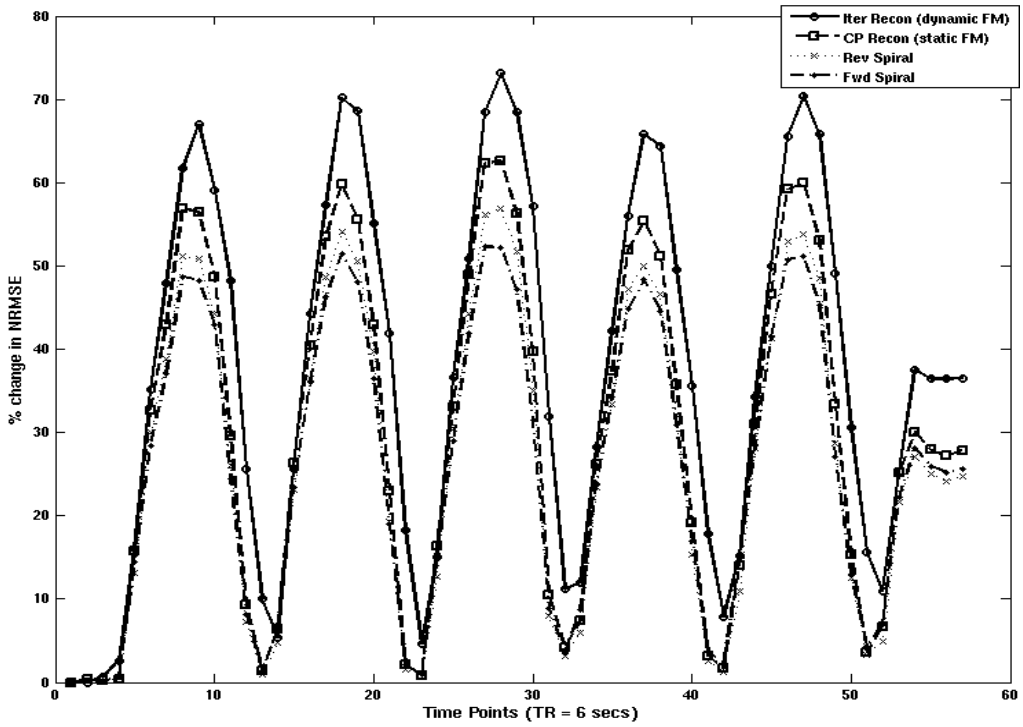

Figure 3-5: For a representative 5mm dataset for human experiments, iterative reconstruction with dynamically updated fieldmaps result in best quality of motion correction as indicated by the consistently higher percentage reduction in NRMSE compared to CP reconstruction with static fieldmap and followed by reverse spiral only and forward spiral only datasets. All of the images for the included time series were reconstructed from the same k-space trajectory.

Functional Studies

METHODS: The subjects were asked to rehearse a motion paradigm under supervision of the researcher prior to the scan. According to this paradigm, the subjects were instructed to keep the extent of head displacement as consistent as possible across scans to limit the range of motion. Each trial consisted of a visual stimulus - alternating checkerboard @ 8 Hz - while performing a motor - bilateral finger tapping - task. Individual trials consisted of 5 cycles of 20 s active task-performing (stimulus on) periods followed by 20 sec of control or rest period consisting of fixation at a cross in the center of a grey screen.

During each trial, six subjects were instructed to either a) hold their head still or b) performed calibrated movements according to instructions provided before the study. The rest and motion experiments were ordered randomly. For each subject, images were acquired using a GRE sequence with TR=2 s, TE=27 ms, FOV 24 cm, data matrix [64 X 64] with in-plane resolution of (3.75 mm X 3.75 mm) with forward spiral only and combined forward and reverse spiral acquisition schemes. All human subjects were scanned with informed consent approved by the University of Michigan's Internal Review Board.

RESULTS: Of the six subjects scanned, data from one of the subjects had to be excluded as the subject was not able to complete the scan. For the remaining subjects, the number of active pixels detected (threshold $Z \geq 4.0$), after motion correction (for studies with intentional motion), was compared across k-space acquisition methods – forward/reversed/combined forward and reversed spirals, and reconstruction methods; reconstruction methods – CP gridding reconstruction with static fieldmaps/iterative reconstruction method with jointly estimated and dynamically updated fieldmaps.

A representative dataset is shown in **figure 3-6**. Iterative reconstruction with dynamically updated fieldmaps performed the best, both in terms of image quality and number of active voxels detected at rest and in presence of large head motion (>2 deg & >3 mm). Among CP gridding reconstruction methods with static fieldmaps, combined reverse and forward spiral method was able to detect the most number of active voxels compared to forward only or reverse only with the forward only reporting the smallest active region. Forward spiral only showed significant distortions and loss of signal due to susceptibility artifacts in functional images, while the iterative reconstruction with dynamic fieldmap seemed to best preserve the fidelity of the images.

It is worth noting that for the representative case included in **figure 3-6**, the overlap between active voxels detected during experiments without motion and, with head motion, is quite large for iterative reconstruction with dynamic fieldmaps compared to the CP reconstruction method with static fieldmap. Both methods used the exact same k-space data.

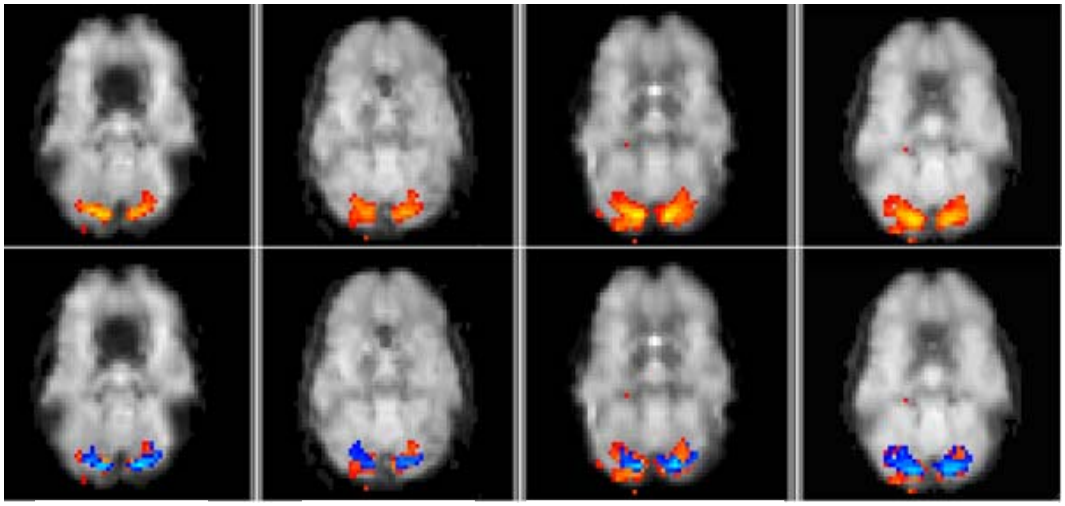

Fwd Spiral CP (Static)	Rev Spiral CP (Static)	Fwd & Rev Spiral CP (Static)	Fwd & Rev Spiral Iter (Dynamic)

Figure 3-6: A 6mm slice from lower brain region. **Top row** - functional maps with no motion (red) and bottom row - active voxels recovered (blue) after motion correction of movement corrupted scans. Note: In the bottom row, the blue voxels are superimposed on active red voxels from scans with no motion. Iterative reconstruction with dynamic fieldmaps performs the best, both in terms of image quality and recovery of active voxels in presence of motion. Among CP gridding methods with static fieldmaps, combined forward & reversed spiral performs the best followed by reversed spiral and then forward spiral respectively. In this case, iterative reconstruction method is able to restore almost all of the pixels in this case, despite large head motion.

The total number of active voxels recovered for all six volunteers across slices of different thickness, different acquisition and reconstruction methods in presence of motion is presented in **figure 3-7** and presented for each subject in **table 3-2**. In general, iterative reconstruction method with dynamic fieldmap detected most number of active pixels in control (rest) cases and, also the largest number of active pixels after motion correction for a similar VOI spanning multiple slices in the lower regions of the brain. For all subjects and experiments, approximately similar VOIs were selected by visual inspection of the lower regions of the functional images most affected by susceptibility artifacts because of its proximity to the frontal and temporal sinuses. Among methods

using static fieldmaps, combined forward and reversed spiral CP gridding reconstruction was more robust to motion induced dynamic changes in susceptibility artifacts followed by reversed spiral and forward spiral CP gridding reconstruction methods respectively.

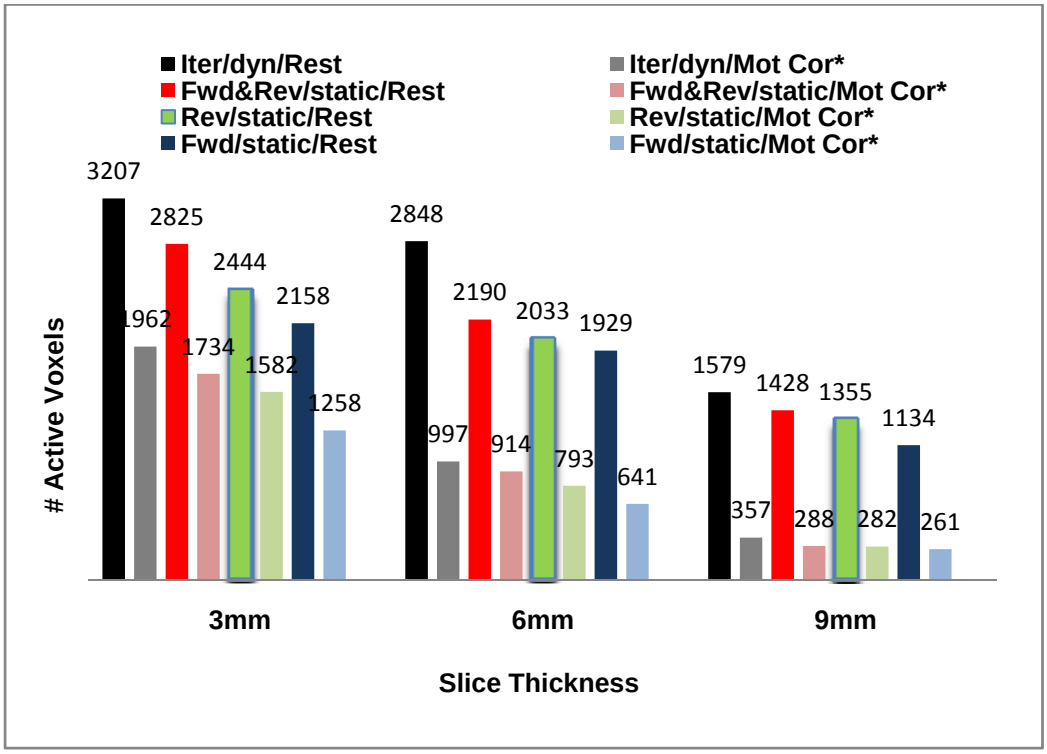

Figure 3-7: Combined result for six subjects across different slice thickness. Of all acquisition and reconstruction methods and across all slice thicknesses, iterative reconstruction with dynamic fieldmaps is able to detect and maintain larger number of activating pixels for studies with motion. Of the methods with using static fieldmaps, the combined forward and reversed spiral acquisition performs better than reversed only and forward only acquisitions respectively.

Table 3-2: Number of active voxels for studies without motion (Rest) and voxels detected after motion correction for studies with motion (Mot Cor*) for six subjects across different slice thickness. Of all methods iterative reconstruction with dynamic fieldmaps is able to detect and maintain larger number of activating pixels for studies with motion. Of the methods with using static fieldmaps, the combined forward and reversed spiral acquisition performs better than reversed only and forward only acquisitions respectively.

	Iterative/dynamic FM		Fwd&Rev/static FM		Fwd/static FM		Rev/static FM	
Subject #	Rest	Mot Cor*	Rest	Mot Cor*	Rest	Mot Cor*	Rest	Mot Cor*
[3mm]								
#1	366	330	339	326	180	215	212	239
#2	539	248	428	225	273	163	194	138
#3	530	436	487	361	484	366	383	306
#4	372	78	366	70	323	88	354	69
#5	1045	793	876	677	879	676	753	437
#6	355	77	329	75	305	74	262	69
[6mm]								
#1	267	189	266	179	166	115	140	111
#2	432	199	444	194	393	124	285	118
#3	299	146	247	140	246	139	242	116
#4	203	120	189	93	180	103	183	92
#5	1255	333	729	299	733	301	783	204
#6	392	10	315	9	315	11	296	0
[9mm]								
#1	97	83	99	76	79	42	67	53
#2	280	14	281	10	222	18	178	12
#3	133	38	101	38	98	38	99	25
#4	105	78	77	50	91	72	82	49
#5	728	109	675	82	670	80	533	92
#6	236	35	195	32	195	32	175	30

3.4 Discussions and Conclusions

Use of combined forward & reverse spiral acquisition method proved to be better than forward only & reverse only acquisition methods, both, in terms of quality of image

registration and preserving the fidelity of areas of task induced activation during fMRI studies with head motion. Combined forward and reverse spiral acquisition is generated by averaging of two datasets; data from the forward spiral and the reverse spiral. This averaging results in improved quality of images by increasing SNR at none to minimal penalty on temporal resolution as little to no extra time is required to acquire the additional forward (or reverse) k-space data. Further, combined forward and reverse spiral is more robust to susceptibility and motion artifacts than forward spiral and, more sensitive to BOLD contrast compared to reverse spiral. Thus, forward and reversed spiral acquisition method is highly beneficial in studies with head motion that leads to erroneous contributions to image from in-plane gradients. These artifacts might change unpredictably for each subsequent time point increasing the variability and reducing the sensitivity of the fMRI studies.

Compared to CP gridding reconstructions with static fieldmaps, use of iterative reconstruction and dynamically updated fieldmaps result in significant improvement in quality of images and motion correction in phantom and human studies. Use of dynamically updated fieldmaps increases the robustness of fMRI studies in presence of head motion by more accurately compensating for the artifacts from temporally changing B_0 inhomogeneity.

In functional studies, higher number of active voxels were detected with use of iterative reconstruction with dynamic fieldmaps both, in case with motion (and motion correction) and without motion. This indicates that use of this method is generally more beneficial compared to other CP reconstruction methods that use static fieldmaps. However, our data does provide conclusive evidence that iterative reconstruction with

dynamic fieldmaps was more effective, compared to CP reconstruction methods, in compensating for motion related field inhomogeneity changes in the regions of activation. This might be due to a number of factors. The extent of the motion might not be large enough to realize the benefits from use of dynamic fieldmaps or, the active regions, in this case the visual cortex, might be located in areas which are perhaps not affected by motion related field inhomogeneity effects. Further experiments need to be carried out in this regard to investigate the benefits of use of dynamic fieldmaps in increasing the sensitivity of fMRI studies, specifically in presence of motion induced distortions or artifacts.

Despite the advantages, iterative reconstruction and joint estimation of fieldmaps at every time point require resources and computational time that are orders of magnitude larger than the CP gridding reconstruction methods with static fieldmaps. However, in presence of head motion where the susceptibility artifacts change dynamically, the benefits from using iterative reconstruction with dynamic fieldmaps certainly present a compelling argument for their increased use.

CHAPTER 4

Post-Processing Methods: Removal of Residual Motion Artifacts using Constrained Independent Component Analysis

4.1 Background and Theory

Of many available fMRI protocols, BOLD fMRI that uses the susceptibility difference between oxygenated and de-oxygenated hemoglobin as a natural contrast agent is most prevalent [22, 68]. BOLD fMRI has lead to numerous insightful discoveries into structural and functional organization of the brain by enabling investigators to non-invasively observe the underlying physiology and neuro-vascular mechanisms using MR images. However, the full potential of BOLD fMRI (and to a large extent, other fMRI protocols as well) is yet to be realized due to several artifacts and confounds that limit its accuracy, specificity and sensitivity.

In BOLD fMRI physiologically induced contrast ranges between only 1 to 5 percent. Signal changes from structured and unstructured noise sources - head motion leading to "spin history" effects [2] and dynamic field inhomogeneity artifacts [7, 8], physiological noise both, cardiac and respiratory [69-72], interpolation errors from image registration [10, 11], machine noise and others [1, 3, 4] – can easily exceed this amount and make it difficult to separate BOLD signal from artifacts. Moreover, many of these artifacts are not corrected by image registration. In this chapter, we will focus our efforts

on removing or mitigating the impact of residual motion artifacts that remain in the fMRI time series data post image realignment and, potentially can be a major source of unaccounted variance in fMRI time-series.

Even the most accurate of image registration methods only correct for bulk movements while leaving the secondary artifacts untouched. Left uncorrected, these secondary artifacts cause erroneous and complex image intensity modulation in the images that can be linear as well as complex non-linear functions of motion. The resultant variance in the fMRI time-series reduces the specificity, accuracy and sensitivity of detection of active voxels. Recently, there have been quite a few studies that emphasize the utility of modeling and removal of residual motion artifacts. Grootoonk et. al. [11] used a Principle Component Analysis (PCA) method to model and regress out image interpolation error under controlled linear translations in y and z directions. Further, the use of Nuisance Variable Regression (NVR) method by Lund et. al., [57] underscores the necessity for removing structured noise from fMRI dataset. In their study, Lund et. al., showed significant improvements in detection of activating voxels by using well characterized models of drift, physiological noise, phase jitters in Hemodynamic Response Function (HRF) as NVRs in the GLM design matrix and correcting for the errors from these structured noise. The inclusion of motion parameters as NVRs further improves the number and statistical power of detected active voxels but, this method seems inadequate in resolving all motion related residual artifacts. In their systematic study of use of motion parameters as NVRs or "Nuisance Explanatory Variables" (NEVs), Jonhstone et. al. [59] contend that the improvements in the sensitivity of detection of activating voxels is observed only in selective cases. Note, NEV and NVR

are different terminologies used by different authors to refer to the same process of using noise models (e.g., motion parameters, cardiac and respiratory time courses) as nuisance regressors to remove erroneous contribution to the data in a linear regression framework. There is also an active push towards using non-parametric data driven methods to isolate and remove these residual motion artifacts. In general, most of the current methods that account for residual motion artifacts during post-processing of images fall into two main categories: General Linear Model (GLM) and Data Driven or Component Based Models that include PCA, Independent Component Analysis (ICA) and others.

4.1.1 General Linear Model (GLM)

The model-based methods use estimated rigid body motion parameters or some combination of these parameters, physiological artifacts and other known sources of errors as NEV in a GLM framework [GLM+NEV] [59, 73, 74] and try to regress out erroneous contributions from head motion post realignment. The activation signal received during BOLD fMRI, $\boldsymbol{b}$, is modeled by:

$$\boldsymbol{b} = \boldsymbol{X\beta} + \boldsymbol{S\delta} + \boldsymbol{N\gamma} + \boldsymbol{\varepsilon} \tag{4.1}$$

where, $\boldsymbol{X\beta}$ is the response to the stimulus provided, $\boldsymbol{S\delta}$ represents the constant and linear drift terms, $\boldsymbol{N\gamma}$ is the NEVs including motion parameters obtained from image registration or external monitoring and, possibly, physiological noise models measured from external devices or estimated and modeled from k-space or image data. Having modeled and removed various sources of errors and artifacts modeled above, the "corrected" fMRI data is processed statistically to detect functionally active voxels.

Although GLM+NEV methods improve the sensitivity of detection of fMRI in many cases, they have their limitations. Besides being confounded by the accuracy of the available model or explanatory variables, they remove erroneous components that are only linear functions of motion parameters. Many sources of the secondary artifacts, for example, the dynamic interactions between motion and susceptibility induced field inhomogeniety that are non-linear and cannot be effectively modeled by simple linear regression. Further, if the motion is even slightly correlated to task, the GLM+NEV methods can be particularly vulnerable as they tend to be conservative and miss classify truly active voxels as caused by motion and related intensity modulations. Overall, GLM based methods are limited in their effectiveness in removing or reducing the impact of residual motion artifacts.

4.1.2 Data Driven or Component Based Methods

An alternative to model based methods, data-driven component analysis methods such as PCA [11, 75] or ICA [76-79] are increasingly being considered for isolation and removal of residual error components. The component-based methods are not model dependent and circumvent many of the limitations of GLM based methods. As such, data-driven methods are more effective in isolating residual erroneous components. While PCA is more suited to reducing variance from unstructured noise, ICA is better able to isolate structured noise - artifacts that are related linearly or non-linearly to a common underlying source such as motion or physiological noise, cardiac, respiratory motion etc. [76]. Given that we are considering removal of more structured noise from motion, we chose to investigate ICA as a preferred method for removing residual motion artifacts in this study.

4.2 Independent Component Analysis

Use of ICA as a method for isolation and removal of residual motion artifacts and other secondary artifacts has been shown to be very effective in many studies, especially when the errors arise from distinct and statistically independent sources [76, 77, 79]. The underlying **ICA** model assumes that there are **'n'** statistically independent sources that have been mixed linearly into **'n'** output signals. Thus, the received signal, **X = [X1; X2; .. Xn]** results from linear mixing of the original and statistically independent sources or components, **S = [S1; S2; .. Sn],** via a mixing matrix **A**. This process can be represented as:

(4.2) $\mathbf{X}_{nx1} = \mathbf{A}_{nxn}\mathbf{S}_{nx1}$**;**

The original signal, **'S'** and the mixing matrix **'A'** are both unknown. Assuming that the underlying sources are statistically independent, one tries to iteratively estimate an unmixing matrix, **'W'**. For example, at the i^{th} step of the iterative algorithm, the unmixing matrix W_i is updated in a way so as to maximize a measure of statistical independence of the estimated sources, s_i given by $s_i = W_i\mathbf{X}$. Various measures of statistical independence can be used to formulate the cost function for the iterative method. Some commonly used ones include mutual information (MI), entropy, negentropy and others. After the algorithm converges (or stopping criteria is reached), the final estimate of **'$\underline{\mathbf{W}}$'** is usually an approximation of the inverse of '**A**' i.e. **[A*$\underline{\mathbf{W}}$ ~ I]**. Having estimated the unmixing matrix, the original source of the signal is then calculated as:

(4.3) $\underline{S} = \underline{W}^{*}X;$

The underlying sources $\underline{S}_{nx1}$ estimated at the end of this process are approximately statistically independent. Further details on ICA in general can be found in an excellent reference [80]. A pictorial representation of the basic ICA estimation process is shown in **figure 4-1**.

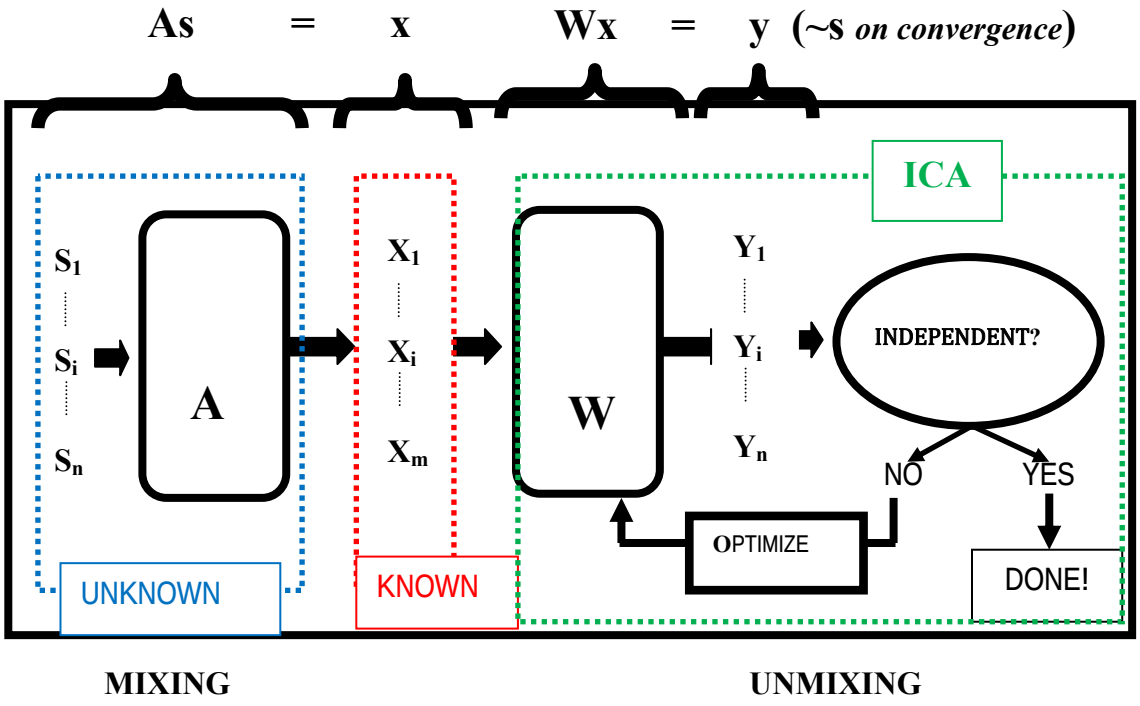

Figure 4-1: The "**unknown"** section of the figure shows the original sources (S_1 .. S_n) being mixed by a process (mixing matrix) '**A'**. The "**known"** section represents the observed signal from which the unmixing matrix **W** and estimate of sources, ($Y_1..Y_n$), need to be derived. After setting a random initial '**W**', estimate of sources, ($Y_1..Y_n$), are calculated iteratively. The iterations proceed by maximizing the statistical independence of estimated sources ($Y_1..Y_n$). The **W** at the end of the iteration process is the estimated unmixing matrix used to estimate the original source as shown in equation **4.3**. (**Adapted from reference [81]**.)

4.2.1 ICA in context of fMRI

In fMRI, the most commonly used ICA method involves resolving the entire fMRI data into two distinct entities. One of the entities consists of the spatial

components or spatial maps of voxels located within the imaged volume. These voxels are the source of the generated signal. For example, one component might include a collection of all the active voxels in the visual cortex that respond to visual stimuli during an fMRI study while another component might include collection of voxels affected by intensity modulation from head motion.

The other entity contains the time courses or information regarding the temporal evolution of the signal from respective sources or components. In the context of ICA as described in equation **4.3**, the spatial voxel maps would form source signals, **S**, and the time courses would be represented by the columns of mixing matrix **A**.

As shown in the **figure 4-2**, initially each of the 3D image volume (of dimension $\boldsymbol{N^3}$) is collapsed into a single row and stacked into a matrix where each row contains the entire imaged volume at a particular time point. The data from the entire fMRI time series (of $\boldsymbol{k}$ scan repetitions) are stacked into a 2D matrix in the manner described above where each row represents the collapsed image volume and the temporal information is captured along the column direction. To put things in perspective, the observed data in this case will be a data matrix of dimension $\boldsymbol{k}$ ***by*** $\boldsymbol{N^3}$.

After performing ICA on the data, the inverse of the unmixing matrix **W** (or estimate of the mixing matrix, **A**) contains the time courses of the corresponding spatial component map in the image coordinates. This is usually referred to the spatial ICA in fMRI. It is possible to perform temporal ICA in fMRI as well by simply transposing the data i.e., stack the image data along the columns and let each row represent the temporal evolution of a single voxel.

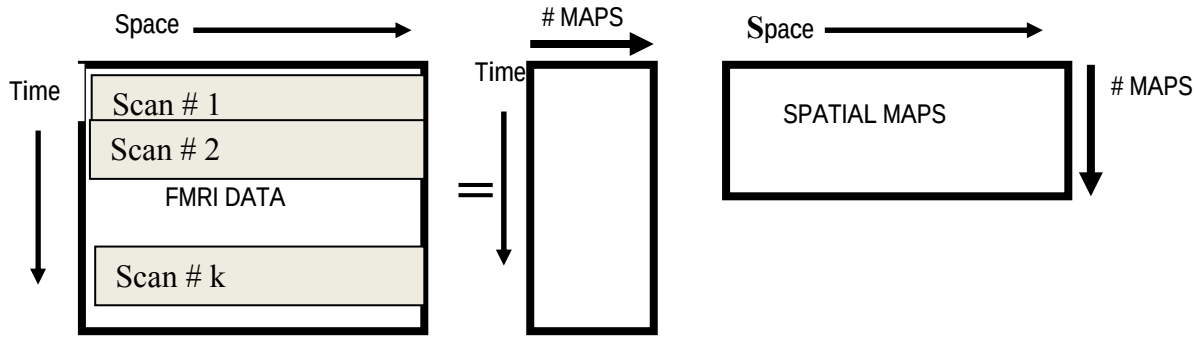

Figure 4-2: Spatial ICA for fMRI. The combined observed dataset of dimension $\boldsymbol{k}\mathbf{x}\boldsymbol{N}^3$ is resolved by ICA into the spatial maps or components (each of dimension $\boldsymbol{1}\mathrm{x}\boldsymbol{N}^3$) that are the source of the fMRI signal and a mixing matrix **A** that contains the time courses (each of dimension $\boldsymbol{k}\mathbf{x}\boldsymbol{1}$) of these spatial maps.

Use of ICA to remove residual motion artifacts from fMRI data series is a two stage process. It involves the isolation of fMRI data into various components as shown in **figure 4-2**. Then, residual motion components need to be identified and removed from the dataset. The identification step can be tedious and time consuming as one has to manually inspect or use some pre-determined similarity measure between motion parameters and the time course of all the components [76]. Despite this drawback, ICA does have a significant advantage in that ICA is better able to isolate components that are related to motion possibly in a complex non-linear and unpredictable fashion, something that is not possible with GLM based methods. Such non-linear interactions might arise from susceptibility induced field inhomogeneity changes with motion, interpolation artifacts and other structured noise. Thus, ICA is potentially a more effective and complete method of correcting for residual motion artifacts and reducing variance in the fMRI time series compared GLM+NEV or even PCA.

4.2.2 Constrained ICA (cICA)

Within the context analysis of fMRI data using ICA, there are two distinct types of constraints that can be considered: **temporally constrained ICA** or **spatially constrained ICA** in fMRI. As described above, the columns of matrix, **A** ($\simeq \mathbf{W}^{-1}$), represent the time courses or temporal evolution of respective components or sources, **S**. Placing constraints on column(s) of '**A**' leads to temporally constrained ICA and, imposing constraints on structure of estimated sources of signal, '**S**' leads to spatially constrained ICA in fMRI. In interest of completeness, the theory and implementation of both the algorithms will be briefly described in below.

4.2.3 Spatially constrained ICA in fMRI

During ICA, one might place constraints on the estimate of the sources or components, '**S**', e.g., when the sources being estimated have a known structure or characteristic. Consider a signal $\boldsymbol{v} = [v_1, v_2, .. v_k]^T$; to be a linear combination of statistically independent sources, $\boldsymbol{s} = [s_1, s_2, .. s_t]^T$. The mixing and the unmixing process can be represented respectively as:

(4.3) $v = As; \quad s = Wv;$

where ***'A'*** and ***'W'*** are the mixing and unmixing matrices respectively. Note that for the included example, the mixing is assumed to be square – the number of estimated sources, $s_1, .. s_t$, equals the number of observed signal, $v_1, .. v_k$, i.e. ($t=k$). However, there is no such restriction in general ICA methods. In fact, one of the most common assumptions for use of ICA in fMRI is that there are fewer sources than observed data ($t<k$). As such,

appropriate dimensionality reduction methods are used to reduce the dimensions of collected data before estimating the underlying independent sources or components [79].

As stated earlier, there are many contrast or cost functions that represent a measure of statistical independence of sources being estimated and can be used for optimization during the estimation of the unmixing matrix, ***'W'***. The use of negentropy ***J(y)*** [80], will be discussed in detail because negentropy is contrast function used by the FastICA [82], the algorithm that has been extensively used during this study. Negentropy is defined by:

(4.4) $$J(y) = H(y_{gauss}) - H(y)$$

Where **H(.)** is the differential entropy and $\mathbf{y_{gauss}}$ is a Gaussian random variable (RV) with the same variance as output signal **y**. Maximizing the negentropy of the estimated signal during the iterative estimation process produces the Independent Components (ICs) [82]. Negentropy is always nonnegative and if **y** is a Gaussian RV, then negentropy is zero. A flexible, reliable and computationally efficient approximation of negentropy is provided by Hyvarinen et. al. and is represented as [82]:

(4.5) $$\boldsymbol{J(y) \approx \rho\{E[G(y)] - E[G(v)]\}^2}$$

Where, **ρ** is a positive constant, **v** is a zero mean, unit variance Gaussian RV and **G(.)** is chosen from a set of quadratic functions depending upon assumptions of the distribution of the signal being estimated as either sub-gaussian or super-gaussian. Maximizing this contrast function described in equation **4.5** leads to estimation of Independent Components using the FastICA method which is currently the most commonly used method for ICA estimation.

If apriori information regarding the structure of the source/component being estimated is available, then this information can be introduced as an additional constraint, apart from the maximization of the negentropy to estimate the ICs, during the iterative estimation process of fastICA. For example, if we know that one of the sources has a structure similar to an available reference function, **r**, one can constrain the estimation process to estimate an IC that is independent from other components while also being most similar to the provided reference function, **r**.

A simple correlation, $\boldsymbol{\epsilon(\mathbf{w})}$, was used as a measure of similarity between the reference signal, **r** and the estimated source. The component estimated in this manner might not be a perfect match to **r** and, one might be able to adjust the threshold parameter, $\boldsymbol{\varepsilon}$, to enforce the degree of similarity between the estimated source and reference. The similarity constraint can now be formulated as:

(4.6) $\boldsymbol{g(w) = \epsilon(w) - \varepsilon \leq 0}$;

where **w** denotes a single demixing vector (corresponding to a single column of demixing matrix '**W**') such that estimated component, $\boldsymbol{y = w^T v}$; and, $\boldsymbol{g(w)}$ represents the closeness between the output **y** and reference signal **r**. Note, the constraint is expressed as a function of "**w**" since **w** is the only quantity that is updated at each step and, estimation of **y** depends on **w**. The measure of closeness between **r** and **y** $\boldsymbol{(= w^T v)}$ can be mean squared error, correlation and many other such measures of similarity between the source and reference. With the constraints placed, the cICA problem is then modeled as detailed in reference [18]:

(4.6) Maximize : $\boldsymbol{f(w) = \rho\left[E[G(y)] - E[G(v)]\right]^2}$;

Subject to: $\boldsymbol{g(w) \leq 0;\ h(w) = E[y^2] - 1 = 0;\quad E[r^2] - 1 = 0;}$

Where **f(w)** denotes the contrast function (negentropy in this case), **g(w)** is the similarity constraint, **h(w)** is the unit variance constraint placed on such that the output **y** has unit variance, and the reference signal is also constrained to have unit variance. This constrained optimization problem is then solved by an augmented Lagrangian method where a Newton-like learning process is used for estimation of Lagrangian parameters and learning of the weights during the progress of the iterative optimization algorithm that updates **w** at each step. For further details, please see the reference [];

It is possible to use the above described algorithm to estimate temporally constrained ICA for fMRI by reversing the dimension in which the received data from fMRI study is arranged during the ICA estimation process. In this case, the **A** matrix would represent the spatial maps, and the estimated **S** would represent the time courses. However, considering the large dimension of the images, for example N^3 where $N=64$ for a typical fMRI study, compared to the small number of time points (~100) collected in fMRI studies, significantly more computing resources would be required to calculate and manipulate a variance matrix for temporal fMRI [$O(N^3XN^3)$] than spatial ICA in fMRI [$O(\sim 100X100)$]. As will be seen in the next section, we took a different approach to temporally constrained ICA was to avoid the issue.

4.2.4 Temporally constrained ICA

Temporally constrained ICA in fMRI is based on a philosophy similar to that of the spatially constrained ICA. For the purpose of this work, the same basic ICA algorithm, FastICA was used to estimate the components. However, instead of

constraining the estimated components to be close to a reference function **r**, as described in equation **4.6**, the algorithm instead updates the columns of the unmixing matrix **W or** $(\mathbf{A}^{-1})$ to be similar to the provided "reference" (e.g. task waveform, motion parameters, cardiac or respiratory time courses), thereby forcing some similarity between the temporal structure of the estimated components and the provided reference.

A summary of temporally constrained FastICA implementation used as a part of this work is provided in the pseudo-code below [83].

TEMPORALLY CONSTRAINED ICA

STEP: Initialization:

1. ***Given:***

$\boldsymbol{z(t)}$, *the whitened observed signal*
$\boldsymbol{V}$, *the whitening matrix*
$\boldsymbol{A_c}$, *the columns of mixing matrix* $\boldsymbol{A}$ *with apriori known temporal structure*

2. ***Form:***

$\boldsymbol{H_c}$, *collection of whitened and orthonormal columns of constrained time-courses by multiplying by the whitening matrix and orthonormalizing:*

$\boldsymbol{H_c = VA_c}$ *and orthonormalize.*

3. ***Setup:***

Then Set $\widetilde{\boldsymbol{H}} = [\widetilde{\boldsymbol{H}}_{\boldsymbol{c}}, \widetilde{\boldsymbol{H}}_{\boldsymbol{u}}]$ *with* $\widetilde{\boldsymbol{H}}_{\boldsymbol{c}} = \boldsymbol{H_c}$ $\boldsymbol{H_u}$ *initialized to random values and orthonormalize* $\widetilde{\boldsymbol{H}}$ *while preserving columns of* $\widetilde{\boldsymbol{H}}_{\boldsymbol{c}}$.

STEP: Independent Column Update:

1. ***Update estimates of cols of*** $\widetilde{\boldsymbol{H}}$ ***using a Newton-like gradient descent algorithm and, negentropy based contrast function [Equation 4.5]:***

$$\widetilde{\boldsymbol{h}}_{\boldsymbol{u},i} \leftarrow \boldsymbol{E}\left\{\boldsymbol{z(t)}\boldsymbol{g}\left(\widetilde{\boldsymbol{h}}_{\boldsymbol{u},i}^{\boldsymbol{T}}, \boldsymbol{z(t)}\right)\right\} - \boldsymbol{E}\left\{\boldsymbol{g}'\left(\widetilde{\boldsymbol{h}}_{\boldsymbol{u},i}^{\boldsymbol{T}}, \boldsymbol{z(t)}\right)\right\}\widetilde{\boldsymbol{h}}_{\boldsymbol{u},i};$$
$$\boldsymbol{h}_{\boldsymbol{u},i} \leftarrow \boldsymbol{h}_{\boldsymbol{u},i}/\|\boldsymbol{h}_{\boldsymbol{u},i}\|$$

STEP: SC Column Update:
*(*Updating the constrained columns)*

1. *Modify* $\widetilde{\boldsymbol{h}}_{\boldsymbol{c,i}}$ *of* $\widetilde{\boldsymbol{H}}_{\boldsymbol{c}}$ *with reference to* $\boldsymbol{H_c}$ *using* $\widetilde{\boldsymbol{h}}_{\boldsymbol{c,i}} = \boldsymbol{h_{c,i}}$ ***or some function of*** $\boldsymbol{h_{c,i}}$

IMPLEMENTATION of Algorithm:

Carry out the following iterations until convergence or stopping criterion:

1. ***Apply one IC update to each column of*** $\widetilde{H}$
2. ***Iterative symmetric Orthonormalization of*** $\widetilde{H}$ ***with enforcement of temporal constraints:***
   - **i.** $H \leftarrow \frac{3}{2}\widetilde{H} - \frac{1}{2}\widetilde{H}\widetilde{H}^T\widetilde{H}$
   - **ii.** *Normalize columns of* $\widetilde{\boldsymbol{H}}$ *to unit length*
   - **iii.** *Apply SC updates to the columns of* $\widetilde{\boldsymbol{H}}_{\boldsymbol{c}}$
   - **iv.** *If* $\widetilde{\boldsymbol{H}}$ *is not orthonormal, go to step* $\boldsymbol{i}$
3. ***If not converged, go to step 1.***

In most fMRI studies, time-courses representing the temporal evolution of structured noise sources (such as head motion and physiological noise) are usually easily accessible. In case of head motion, the image registration process yields motion parameters that capture the displacement of the brain over the course of the entire scan period. These motion parameters can be used as references in constrained ICA (cICA) algorithms [83, 84] or semi-blind source separation algorithms [85]. The cICA algorithm preferentially isolates independent components which share the most amount of "similarity" to the provided reference or constraints.

So, the use of cICA eliminates the extra step of manual identification of the artifact components as is common in general unconstrained ICA methods while still affording the advantages of the ICA method. Further, cICA introduces the possibility of automating this ICA-based corrective measure. In this study, we used constrained ICA to combine the isolation and identification of residual motion artifact components into a single step using estimated motion parameters as references for the cICA algorithm. More specifically, we constrained the time-courses (or columns of the un-mixing matrix) of the spatial components to be similar to the six rigid body motion parameters obtained during image realignment. The spatial components isolated by this cICA algorithm were then considered erroneous and removed from the dataset as they are most likely due to head movement.

ICA with constraints described above has been used in MEG studies for identification and removal of structured artifacts [86]. Semi-blind source separation, an idea similar to the elaborated cICA has been used to isolate task related components in fMRI study and has proven to be particularly effective when the time-course of the task related contrast is not accurately known [85]. However, to our knowledge, there has been no study similar to our approach of exploring the effectiveness of "temporally" constrained ICA in removing residual motion artifact and improving sensitivity of BOLD fMRI studies with head motion.

4.3 Methods

Human studies:

Fourteen separate trials were performed by four volunteers who were scanned with informed consent approved by the University of Michigan's Internal Review Board. Each trial lasted 200 seconds and involved a visual stimulus - alternating checkerboard @ 8 Hz - and a motor task - bilateral finger tapping. The trials consisted of 5 cycles of 20 s active task-performance (stimulus on) periods followed by 20 sec of control or rest period. Images were acquired using a spiral GRE sequence with TR=2 s, TE=27 ms, FA = 90 degrees, FOV 24 cm, data matrix [64 X 64] with in-plane resolution of (3.75 mm X 3.75 mm) and, using slice thickness 3 mm, 6 mm & 9 mm. Each volunteer was instructed to intentionally move their head during the scans. These motion corrupted images in the time series were then realigned using the MCFLIRT utility of FSL with the second image in the time series as the reference. Statistical parametric estimation was carried out on the realigned images in four different ways.

i) **GLM:** Statistical parameters were estimated using a GLM as implemented in FEAT utility of FSL.

ii) **cICA:** Six estimated motion parameters were used as references for cICA algorithm to isolate components for which, the time-courses (or columns of the un-mixing matrix) had a correlation to motion parameters that was higher than a pre-determined threshold. These components were then removed and the rest of the data was combined to obtain a time series of images with reduced residual motion artifacts.

iii) **GLM+NEV:** Motion parameters were estimated in a manner very similar to "**GLM"** method, however, the six estimated motion parameters were included as NEVs in the GLM design matrix.

iv) **cICA+NEV:** The data was processed as in **cICA** but, the motion parameters were included as nuisance variables in the GLM matrix for estimation of statistical parameters.

A z-threshold of ≥ 3.5 was used to identify pixels as active. This threshold was chosen after a test retest reliability study described later in this section. Active pixels in the brain were aggregated into a histogram with ten bins over z-scores that ranged between 3.5 up to max z-score value. Number of active pixels at each bin was added cumulatively to generate a graph that showed the incremental number of active pixels at each bin (z-score value) and the total number of active pixels detected thus far – the final data point at the final z-score bin represents the sum of all active pixels. These cumulative graphs were compared across the four analysis methods. A representative sample of cumulative graphs for two independent experiments is shown in **figure 4-3** and the number of active pixels detected for the various methods for all trials are listed in **Table 4-1**.

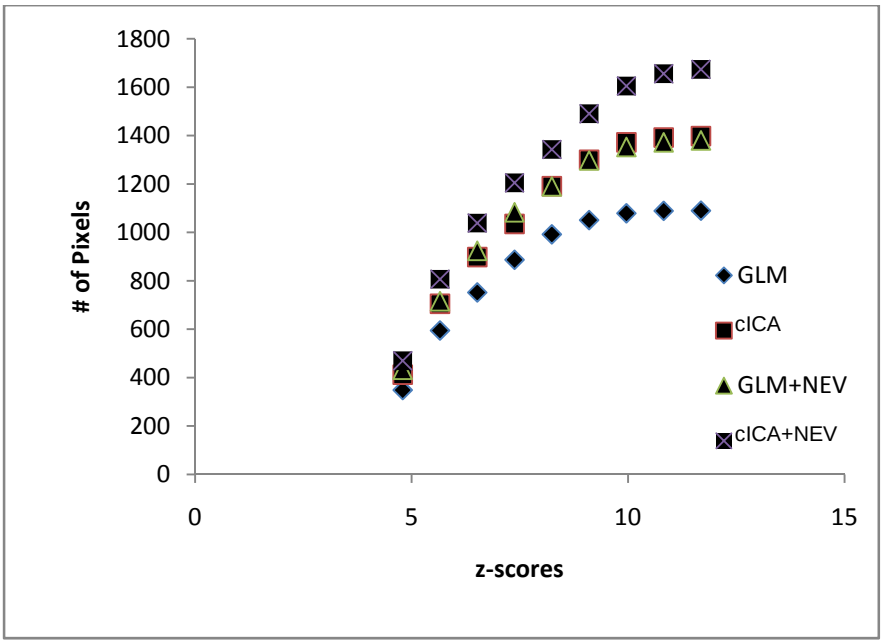

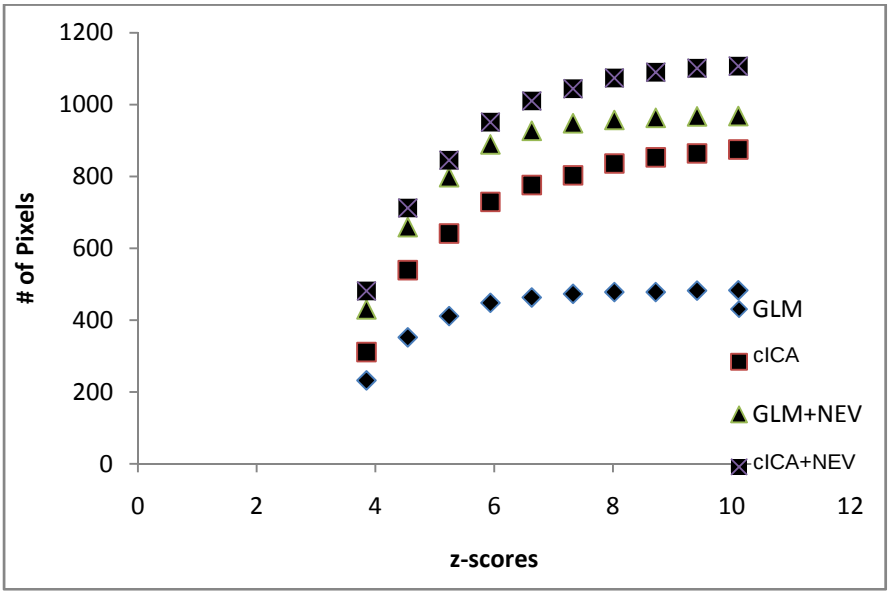

Figure 4-3: shows the cumulative graphs for two representative independent trials from two subjects for various analysis methods. In both, the total number of active pixels and the z-score of individual pixels show prominent improvements with **cICA** compared to **GLM** method. Further, **cICA+NEV** method showed a prominent increase in number of active pixels and z-scores of individual pixels compared to the **GLM+NEV**

Table 4-1: The total number of active voxels detected by four different methods of analysis: GLM, cICA, GLM+NEV and cICA+NEV are tabulated below for all fourteen trials. The total number of active pixels detected by the **cICA** and **cICA+NEV** methods are higher than those detected by the **GLM & GLM+NEV** methods respectively. For five trials highlighted in red, the number of active voxels detected by cICA+NEV method is lower than that of cICA method. This will be discussed in later sections.

Trial #	Total # of Pixels detected			
METHOD	GLM	cICA	GLM+NEV	cICA+NEV
1	1731	2126	2258	2567
2	483	875	968	1107
3	627	643	577	604
4	214	250	438	486
5	170	197	170	240
6	848	1042	900	977
7	201	238	545	610
8	3378	3506	2301	2511
9	952	1118	1305	1369
10	808	829	913	992
11	723	814	425	430
12	1195	1304	1453	1488
13	392	432	334	372
14	712	934	994	1180

The increase in the number of active pixels after using cICA based methods is also shown for a slice from the lower region of the brain where the susceptibility related artifacts are dominant. As seen in **figure 4-4**, cICA increases the number of active pixels detected in the visual cortex compared to the GLM method. Similarly, cICA+NEV method is further able to remove motion related variance and improve the number of active pixels detected in this region.

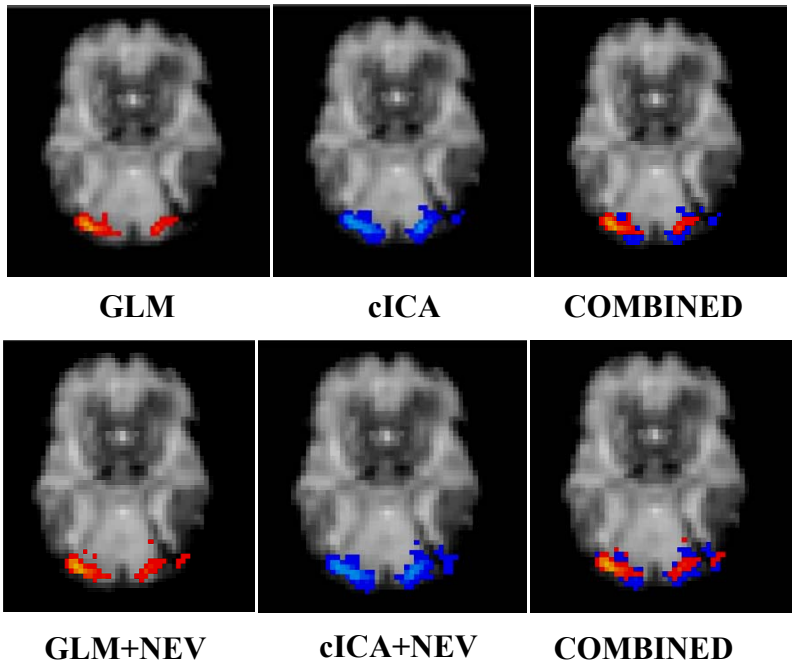

Figure 4-4: (Top row) shows the active pixels detected with the **GLM** (red) vs. **cICA** (blue) [**z≥3.5**] for a slice in the visual cortex near in the lower region of the brain. The combined image clearly shows the additional pixels that are detected when cICA method is used to remove residual motion artifacts. (Bottom Row) compares the **GLM+NEV** (red) vs. **cICA+NEV** (blue) methods. The **cICA+NEV** method performs better than the **GLM+NEV** method. Also, comparing the GLM vs. GLM+NEV methods and cICA vs. cICA+NEV methods shows that the inclusion of motion parameters as NEVs in fact improved the number of active voxels detected.

Removing residual motion artifacts from the dataset using cICA improved the sensitivity of detection of active voxels in almost all trials. The number of pixels classified as active, after processing by cICA, increased significantly as did the z-scores. To ascertain that the increase in the number of active pixels was truly from removal of motion related residual variance and not just increase in number of false positives detected in repeated trials, a receiver operator characteristic (ROC) curve was plotted using the test-retest reliability described by Noll et al. [87]. Four identically repeated trials for one of the volunteers were processed according to the GLM method and analyzed for test-retest activation robustness to generate the ROC. From this curve, a

threshold of z > 3.5 was chosen as a good compromise between the statistical power of detection of active voxels and the false positive error rate (see **figure 4-5**). A more rigorous study of plotting and comparing such ROC curves for all the listed methods, in order to more effectively account for false positive rates, is planned as part of the future work.

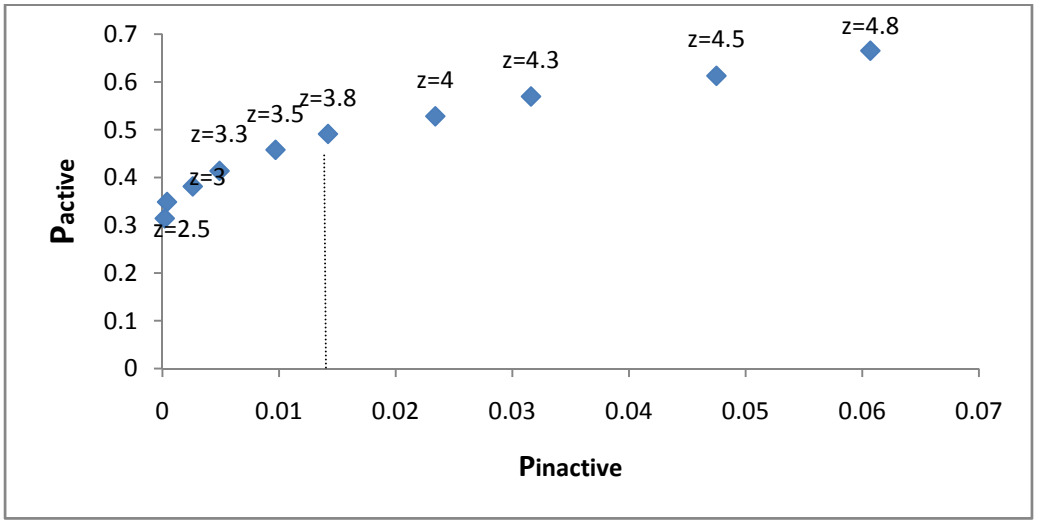

Figure 4-5: The ROC curve which shows plots of Probability of detection of true activation (P_{active}) versus Probablity of detection of false positive ($P_{inactive}$) at the listed z thresholds.

Removal of the six residual motion components, isolated by the cICA algorithm using the motion parameters as references, could potentially bias the subsequent statistical parameter estimation process by reducing the actual degrees of freedom of the dataset as well as modifying the structure of the variance in the data. We additionally analyzed all the datasets by randomly removing six components, other than the components identified as motion related by the cICA and then performing statistical parameter estimation on the resulting dataset. The activation maps from the dataset with randomly removed components and those obtained from the data with only the six

motion related components removed were compared to check if the reduction in degrees of freedom of the dataset had any impact on the sensitivity of detection of active pixels as shown in **figure 4-6**.

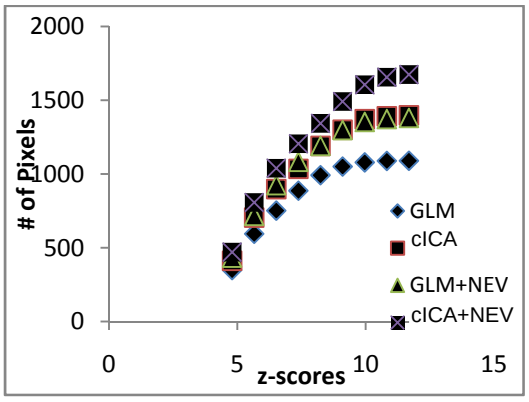

Trial #1: Mot

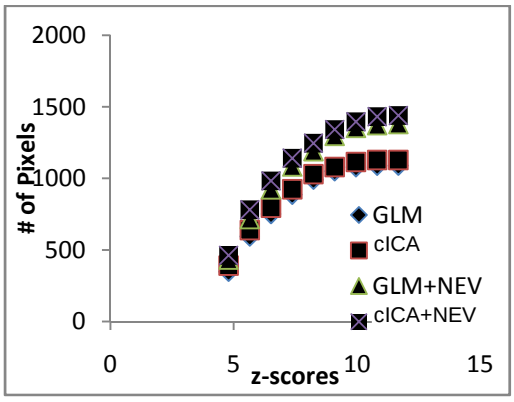

Trial #1: Rand

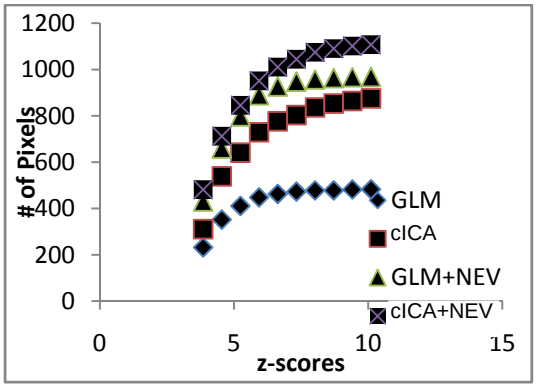

Trial #2: Mot

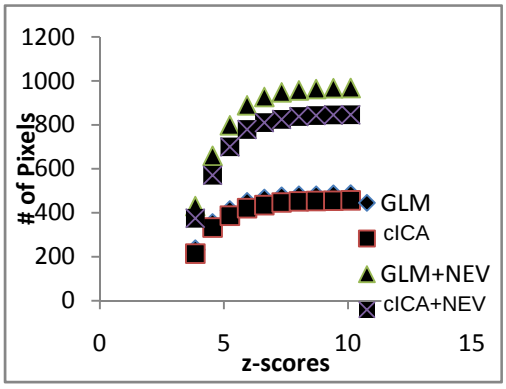

Trial #2: Rand

Figure 4-6: For the two trials shown here, the cICA and cICA+NEV methods show increase in number of active voxels compared to the GLM and GLM+NEV methods when the six motion related components are isolated and removed as shown by the Trial #1&2 (Mot) curves shown in the left column of the figure. When the six random components are removed, for the same dataset, the number of active voxels detected by cICA and cICA+NEV methods are similar or even worse than that of the GLM and GLM+NEV methods.

Table 4-2: The number of active voxels detected by the cICA and cICA+NEV methods are compared across methods which remove the six components randomly versus the six motion related components. As can be seen, the case where the components are randomly removed, the number of active voxels detected decreases invariably compared to the method where the motion related components are removed.

Trial #	Total # of Pixels detected					
Method	GLM	cICA (Mot)	cICA (Rand)	GLM+NEV	cICA+NEV (Mot)	cICA+NEV (Rand)
1	1090	2126	1129	1380	2567	1440
2	483	875	457	968	1107	846
3	627	643	615	577	604	551
4	214	250	227	438	486	467
5	170	197	178	170	240	175
6	848	1042	865	900	977	879
7	201	238	188	545	610	655
8	3378	3506	3354	2301	2511	2399
9	952	1118	878	1305	1369	1119
10	808	829	849	913	992	946
11	723	814	676	425	430	404
12	1195	1304	1146	1453	1488	1368
13	392	432	408	334	372	321
14	712	934	826	994	1180	1159

In five of the fourteen trials conducted, it seemed that inclusion of the motion parameters as the NEVs seem to substantially decreased the number of the voxels detected (see **table 4-1**). This trend was observed in the GLM+NEV and the cICA+NEV methods. We suspected that there might be an appreciable correlation between the task waveform and motion in this case. So, we tabulated the maximum correlation coefficients between the six motion parameters and the task waveform for all the trials and characterized the effect of correlated motion on the number of active pixels detected. These results are included for the five tests for which the inclusion of NEVs reduced the number of active voxels detected.

Table 4-3: The number of active voxels detected by the four methods for all subjects and the maximum correlation coefficient of the motion parameters for each trial.

Trial #	Total # of Pixels detected				Corr w/ Mot Parameter
METHOD	GLM	cICA	GLM+NEV	cICA+NEV	
1	1731	2126	2258	2567	0.0728
2	483	875	968	1107	0.28
3	627	643	577	604	0.42
4	214	250	438	486	0.13
5	170	197	170	240	0.16
6	848	1042	900	977	0.38
7	201	238	545	610	0.06
8	3378	3506	2301	2511	0.57
9	952	1118	1305	1369	0.13
10	808	829	913	992	0.15
11	723	814	425	430	0.39
12	1195	1304	1453	1488	0.22
13	392	432	334	372	0.8
14	712	934	994	1180	0.27

4.4 Results and Discussions

Human Studies:

Comparing the cumulative graphs in **figure 4-3** and the data in **table 4-1**, it can be seen that for all trials, the use of cICA method for isolation and removal of components improved the number of active voxels detected as well as the z-scores of the active voxels when compared to the GLM based methods. This improvement in sensitivity of detection of active pixels indicates that cICA is able to remove residual motion artifacts that might not be corrected in an ordinary GLM based analysis. Further, use of cICA with NEVs

performed better than respective methods that use GLM with NEVs. This result reinforces the idea that the use of constrained ICA is able to capture error components that have a more complex and higher order relationship with head motion than just a linear function that is isolated by using NEVs in the GLM model. As such cICA is a more effective and complete way of isolating and removal of residual motion components compared to the GLM methods that remove only linear effects of the head motion.

To control for the false positive rate, we estimated the test retest reliability parameters using four repeats of the functional scan for a volunteer. A ROC curve for various z-score thresholds was plotted as shown in **figure 4-5.** A z threshold of 3.5 provides a good compromise between true detection rate of P_A=0.47 versus false positive rate of P_I=0.01. An overall z threshold of 3.5 was used for the rest of the study to control for the false positive rate across trials. As stated earlier, a more rigorous control for false positive rates will be undertaken in the future by comparing the differences in ROC curves for each of the four methods listed earlier and setting the thresholds accordingly.

We compared the number of active voxels detected in datasets which were reconstructed after removing the six motion components isolated by cICA algorithm versus the active voxels in datasets where six random components were removed. This was done to ensure the improvement in the z-scores and increase in sensitivity of detection was due to isolation and removal of variance from residual motion artifacts and not just the effect of reducing the degrees of freedom of the dataset. As can be seen in **figure 4-6**, for all the datasets reconstructed after removing six random components, the cumulative curves for cICA show no additional improvements compared to the plots of GLM even though the dataset in question are the same. In fact, the performance of the

cICA based methods even become worse in certain instances. However, as we already saw in **figure 4-3**, removing motion related components isolated by cICA indeed increased number of active pixels detected in all cases. This indicates that the use of constrained ICA with motion parameters as reference truly isolates motion related variance and removes it thereby reducing the variance and improving the sensitivity of detection. Similar trend was observed for all trials as can be seen in **table 4-2** where randomly removing the components decreased the number of active voxels detected compared to the voxels detected after removal of motion related components.

Finally, five of the fourteen subjects showed a decrease in the number of active voxels when the motion parameters were included as NEV, both, for the GLM and cICA cases. The highest value of the correlation coefficient of the six motion parameters and the task waveform for each subject is included along with the number of active voxels detected by each method is included in **table 4-3** was calculated for all subjects and is tabulated. As can be seen, for the five cases (highlighted in red in **table 4-3**), there is at least one motion parameter that has a correlation coefficient greater than 0.3. Thus, a strong correlation of the motion and task leads to removal of the active voxels in a manner that was discussed previously.

4.5 Conclusions

Our studies indicated that in use of cICA to remove residual motion components followed by a GLM+NEV analysis on the resulting time-series is more efficient and effective in isolating residual motion artifacts compared to using just GLM or GLM+NEV method. Use of cICA and cICA+NEV methods is better able to isolate linear and non-linear secondary image artifacts. This is evident from increased active

pixels detected in the lower brain slices. If left uncorrected, residual motion artifacts from motion induced field inhomogeneity changes are more likely to contribute to larger variances in time series in these lower slices and reduce sensitivity of detection. Further, cICA does not require an additional step of manual identification of the error components as with use of ICA only. In conclusion, cICA method significantly improves the sensitivity of detection of active pixels compared to GLM or GLM+NEV methods and, it does so more efficiently than traditional ICA methods.

CHAPTER 5

Conclusions and Future Work

5.1 Conclusion

Head motion still remains a major confound in fMRI despite a great deal of effort and resources devoted by the fMRI community to improving motion correction algorithms. Although accurate image registration algorithms are critical, correction of secondary motion artifacts is just as important if one were to improve the accuracy and expand the capabilities of fMRI in presence of head motion. This study was aimed at increasing the robustness of fMRI to secondary artifacts from head motion and also to effectively remove these artifacts where unavoidable. As can be seen in chapters 2 and 3, some already existing methods that improve MR image quality in general were modified and adapted to improve robustness of MR images to motion. Further, in chapter 4, a novel technique to remove the residual artifacts from head motion was used effectively. These methods and interventions together increased the accuracy, specificity and sensitivity of fMRI studies.

5.1.1 Contributions

We explicitly optimized acquisition parameters and used improved reconstruction methods to make fMRI more robust to secondary motion artifacts. Further, use of data-

driven constrained ICA method for isolating and removing residual motion artifacts further increased the accuracy and sensitivity of fMRI experiments. The unique contributions of this work are listed below:

Acquisition Parameters: Use of thinner slices improved the robustness of MR images to susceptibility and motion artifacts and improved the quality of motion correction in phantom and human experiments. No conclusive evidence emerged regarding the impact of thinner slices on sensitivity of detection of active voxels in fMRI scan with motion. This might be due to differences in head motion trajectories during data acquisition with thinner versus thicker slices. Functional experiments in this regard need to be repeated using an experimental set up where the motion of the head is consistent and repeatable across scans.

Use of slices of variable thickness for image acquisition improved the signal recovery in the lower regions of the brain most affected by susceptibility artifacts. Variable slice thickness method for acquiring 2D slices combined the benefits from thinner slices while maintaining temporal resolution viable for fMRI studies.

Acquisition and Reconstruction Methods: Use of combined forward and reverse spiral k-space acquisition and iterative image reconstruction with jointly estimated and dynamically updated fieldmaps further improved robustness of MR images to head position dependent dynamically changing susceptibility artifacts. Optimizing the acquisition and reconstruction methods in this manner improved MR image quality and also, the accuracy and completeness of image registration in phantom and human data.

In functional studies, combined forward and reverse spiral acquisition improved the sensitivity of detection of active voxels in fMRI experiments compared to forward only or reverse only acquisitions. Iterative image reconstruction with dynamic fieldmaps detected largest number of active voxels in fMRI experiments with and without motion compared to all other reconstruction methods used. This indicated that the use of this method is beneficial to improving sensitivity of fMRI experiments in general. However, our data did not provide conclusive evidence that iterative image reconstruction with dynamic fieldmaps improves sensitivity of fMRI studies by specifically correcting for the impact of motion on fMRI studies better than other reconstruction methods studied. Further investigation is required to establish the unique benefits derived from use of iterative reconstruction with dynamic fieldmaps in presence of motion.

Artifact Modeling and Removal: Using cICA, we were able to identify, isolate and remove linear as well as non-linear secondary motion artifacts in an automated fashion. Removal of residual motion artifacts improved the sensitivity of detection of active voxels in fMRI studies..

All of these methods improved the sensitivity of detection of functionally active pixels in real fMRI studies Although, the methods investigated above proved effective in enhancing the capability of fMRI as a robust neuro-imaging tool, there are several other corrective measures and intervention that can be explored in the future to further improve the performance of fMRI in presence of head motion. Some of the directions for future

work in this general area are listed below along with some ideas on improving the performance of the methods already listed in detail in the previous sections.

5.2 Future Work

5.2.1 External Tracking Device

An external motion-tracking device can be incorporated in the fMRI setup. Use of such a device will improve the motion estimates and also provide the capability to do real-time prospective and retrospective motion correction. Currently registration algorithms use images to estimate motion and register images to the reference image retrospectively. However, the images in the time series provide inaccurate estimates of the motion parameters as the above described susceptibility effects corrupt the images. Use of external tracking devices will prevent such biased motion estimates and will allow the implementation of real-time prospective motion correction schemes to freeze the motion of the object relative to the scanner frame of reference and avoid errors from image registration steps.

5.2.2 Use of variable Slice-thickness

The use of variable slice thickness for acquiring images shows great promise. We have already shown the benefits from such a method of image acquisition. However, using variable slice thickness in functional studies poses its own set of challenges. These

challenges arise due to differences in SNR in the regions sampled with slices of different thickness and the effect of this SNR variation on motion correction and statistical parameter estimation. SNR from sampling a fixed volume with thinner slices ($SNR \propto V * \sqrt{T_{AD}}$) is reduced by a factor $\sqrt{n}$, where 'n' is the ratio of the dimensions of thicker to thinner slice. For e.g., if a constant volume is sampled with two slices that are half as thick as the original "normal" slice, then the net volume generating the signal i.e., 'V' is reduced by half however, the acquisition time, T_{AD} is doubled as two acquisitions are required to cover the same volume. Thus, there is an overall $\sqrt{2}$ reduction in SNR. There is distinct difference in the net signal intensity of the regions of the images sampled with thinner versus thicker slices. This might cause erroneous motion estimation and correction, especially in motion correction algorithms that minimize the square of image intensity as a metric for image registration. Further, SNR difference might also pose a problem when estimating statistical parameters across regions sampled with different slice thickness. These issues can be further investigated in detail in the future.

5.2.3 Shimming

We have explored using external shimming devices that can be customized for each patient, at the expense of 5-7 minutes at the beginning of each scan, to further improve the quality of signal in the lower regions of the brain and be able to perform functional studies in these regions. This is achieved by placing appropriate material such as stainless steel discs around the region of interest. These discs will modify the

homogeneity of the B_0 field by introducing an additional induction field. By using the off-resonance maps as a measure of field homogeneity and using some optimization scheme to place appropriate number of external shimming entities and at correct location, we have been able to show some improvements in the overall uniformity of the field. A similar study in rats at 9.4 T has shown significant improvements at such high fields [88]. More detailed investigation in this general direction can be undertaken to adapt this method to improve fMRI studies.

5.2.4 Use of Dynamic off-resonance maps in fMRI with motion

Simulation and Estimation: Iterative reconstruction method with jointly estimated and dynamically update field map is able to track and compensate these changes for each time point compared to the CP reconstruction with static field maps acquired at the beginning of an experiment. Although, the ideal would be to obtain high resolution field maps at each acquisition without compromising temporal resolution, it has thus far proven to be an elusive problem. Ways to improve the computational load and accuracy of the joint estimation by using analytical predictions of the field distribution, using motion (independent) motion estimates might be an interesting direction of research in the future.

Investigation of effectiveness of dynamic off-resonance maps: Iterative image reconstruction with dynamic fieldmaps detected largest number of active voxels in fMRI experiments with and without motion compared to all other reconstruction methods used. This indicated that the use of this method is beneficial to improving sensitivity of fMRI experiments in general. However, our data did not provide conclusive evidence that

iterative image reconstruction with dynamic fieldmaps improves sensitivity of fMRI studies by specifically correcting for the impact of motion on fMRI studies better than other reconstruction methods.

In this regard, functional studies need to be designed such that the effect of degree of motion on fMRI sensitivity and accuracy and, the benefits from use of iterative reconstruction with dynamic fieldmaps can be further investigated. Further, the ROI of these functional experiments should be in parts of the brain where field inhomogeneity and motion artifacts have a larger impact on sensitivity of detection of active voxels compared to the visual cortex region used for the scans in this thesis.

5.2.5 Investigating false positive rates in the use of cICA

While use of cICA to remove residual motion artifacts improves the count of active pixels detected, it is important to make sure that this increase in sensitivity is not due to increase in false positives or from bias introduced by the cICA algorithm itself. Experiments can be designed where the subject does not perform any task while still performing head motion. This dataset can then be analyzed with the cICA method and investigated for any "active" voxels. The voxels detected in this manner can be attributed to false activation resulting from biasing of the dataset by the cICA algorithm. This might enable us to determine the true effect of the use of cICA algorithm on the sensitivity of fMRI experiments.

In the results included, an appropriate threshold for the z-statistic was estimated a ROC curve for only the GLM method. Similar ROC curves need to be estimated for all

the other methods, cICA, GLM+NEV, cICA+NEV to compare if the individual methods for their susceptibility to false positives. Further, the effect of reduction of degrees of freedom due to removal of motion related components needs to be more rigorously analyzed.

REFERENCES

1. Hajnal, J.V., et al., *Artifacts due to stimulus correlated motion in functional imaging of the brain.* Magn Reson Med, 1994. **31**(3): p. 283-91.
2. Friston, K.J., et al., *Movement-related effects in fMRI time-series.* Magn Reson Med, 1996. **35**(3): p. 346-55.
3. Zeffiro, T., *Clinical functional image analysis: artifact detection and reduction.* Neuroimage, 1996. **4**(3 Pt 3): p. S95-100.
4. Freire, L. and J.F. Mangin, *Motion correction algorithms may create spurious brain activations in the absence of subject motion.* Neuroimage, 2001. **14**(3): p. 709-22.
5. Jezzard, P., P. Mathews, and S. Smith, *Functional MRI: an introduction to methods*. 1st ed. 2002, New York: Oxford University Press.
6. Storey, P., et al., *Band artifacts due to bulk motion.* Magn Reson Med, 2002. **48**(6): p. 1028-36.
7. Andersson, J.L., et al., *Modeling geometric deformations in EPI time series.* Neuroimage, 2001. **13**(5): p. 903-19.
8. Wu, D.H., J.S. Lewin, and J.L. Duerk, *Inadequacy of motion correction algorithms in functional MRI: role of susceptibility-induced artifacts.* J Magn Reson Imaging, 1997. **7**(2): p. 365-70.
9. Jezzard, P., Clare, S, *Sources of distortion in functional MRI data.* Human Brain Mapping, 1999. **8**(2-3): p. 80-85.
10. Noll, D.C., F.E. Boada, and W.F. Eddy, *A spectral approach to analyzing slice selection in planar imaging: optimization for through-plane interpolation.* Magn Reson Med, 1997. **38**(1): p. 151-60.
11. Grootoonk, S., et al., *Characterization and correction of interpolation effects in the realignment of fMRI time series.* Neuroimage, 2000. **11**(1): p. 49-57.
12. Woods, R.P., et al., *Automated image registration: I. General methods and intrasubject, intramodality validation.* J Comput Assist Tomogr, 1998. **22**(1): p. 139-52.
13. Woods, R.P., et al., *Automated image registration: II. Intersubject validation of linear and nonlinear models.* J Comput Assist Tomogr, 1998. **22**(1): p. 153-65.
14. K. Friston, J.A., C. Frith, J.-B. Poline, J. Heather, and R. Frackowiak, , *Spatial registration and normalization of images.* Hum Brain Mapping, 1995. **3**(3): p. 165-189.
15. Jenkinson, M. and S. Smith, *A global optimisation method for robust affine registration of brain images.* Med Image Anal, 2001. **5**(2): p. 143-56.
16. Jenkinson, M., et al., *Improved optimization for the robust and accurate linear registration and motion correction of brain images.* Neuroimage, 2002. **17**(2): p. 825-41.

17. Cox, R.W., *AFNI: software for analysis and visualization of functional magnetic resonance neuroimages.* Comput Biomed Res, 1996. **29**(3): p. 162-73.
18. Lu, W. and J.C. Rajapakse, *Approach and applications of constrained ICA.* IEEE Trans Neural Netw, 2005. **16**(1): p. 203-12.
19. Jezzard, P., Mathews, PM, Smith, S, *Functional MRI: an introduction to methods*. 1st ed. 2002, New York: Oxford University Press.
20. Ogawa, S. and T.M. Lee, *Magnetic resonance imaging of blood vessels at high fields: in vivo and in vitro measurements and image simulation.* Magn Reson Med, 1990. **16**(1): p. 9-18.
21. Belliveau, J.W., et al., *Magnetic resonance imaging mapping of brain function. Human visual cortex.* Invest Radiol, 1992. **27 Suppl 2**: p. S59-65.
22. Kwong, K.K., et al., *Dynamic magnetic resonance imaging of human brain activity during primary sensory stimulation.* Proc Natl Acad Sci U S A, 1992. **89**(12): p. 5675-9.
23. Torsten Rohlfing, J., B. West, Jürgen Beier, Thomas Liebig Christian A. Taschner Ulrich-Wilhelm Thomale, *Registration of functional and anatomical MRI: Accuracy assessment and application in navigated neurosurgery.* Computer Aided Surgery, 2000. **5**(6): p. 414-425.
24. Belliveau, J.W., et al., *Functional mapping of the human visual cortex by magnetic resonance imaging.* Science, 1991. **254**(5032): p. 716-719.
25. Bandettini, P.A., et al., *Time course EPI of human brain function during task activation.* Magn Reson Med, 1992. **25**(2): p. 390-7.
26. John A. Detre, J.S.L.D.S.W.A.P.K., *Perfusion imaging.* Magnetic Resonance in Medicine, 1992. **23**(1): p. 37-45.
27. Edelman, R.R., et al., *Qualitative mapping of cerebral blood flow and functional localization with echo-planar MR imaging and signal targeting with alternating radio frequency.* Radiology, 1994. **192**(2): p. 513-520.
28. Manus J. Donahue, H.L., Craig K. Jones, Richard A.E. Edden, James J. Pekar, Peter C.M. van Zijl,, *Theoretical and experimental investigation of the VASO contrast mechanism.* Magnetic Resonance in Medicine, 2006. **56**(6): p. 1261-1273.
29. Cohen, J.D., et al., *Temporal dynamics of brain activation during a working memory task.* Nature, 1997. **386**(6625): p. 604-8.
30. Ogawa, S., et al., *Functional brain mapping by blood oxygenation level-dependent contrast magnetic resonance imaging. A comparison of signal characteristics with a biophysical model.* Biophys J, 1993. **64**(3): p. 803-12.
31. Vazquez, A.L. and D.C. Noll, *Nonlinear aspects of the BOLD response in functional MRI.* Neuroimage, 1998. **7**(2): p. 108-18.
32. Schick, F., *Whole-body MRI at high field: technical limits and clinical potential.* Eur Radiol, 2005. **15**(5): p. 946-955.
33. Keith, R.T., *Visual feedback to stabilize head position for fMRI.* Magnetic Resonance in Medicine, 1999. **41**(5): p. 1039-1043.
34. Glover, G.H. and A.T. Lee, *Motion artifacts in fMRI: comparison of 2DFT with PR and spiral scan methods.* Magn Reson Med, 1995. **33**(5): p. 624-35.

35. Shizhe Li, B.J.D., Christopher M. Collins, Qing X. Yang, Michael B. Smith,, *Three-dimensional mapping of the static magnetic field inside the human head.* Magnetic Resonance in Medicine, 1996. **36**(5): p. 705-714.
36. Haacke, E.M., J.A. Tkach, and T.B. Parrish, *Reduction of T2* dephasing in gradient field-echo imaging.* Radiology, 1989. **170**(2): p. 457-62.
37. Noll, D.C. *Rapid MR image acquisition in the presence of background gradients*. in *Biomedical Imaging, 2002. Proceedings. 2002 IEEE International Symposium on*. 2002.
38. Cohen, M.S. and R.M. Weisskoff, *Ultra-fast imaging.* Magnetic Resonance Imaging, 1991. **9**(1): p. 1-37.
39. Peter Jezzard, S.C., *Sources of distortion in functional MRI data.* Human Brain Mapping, 1999. **8**(2-3): p. 80-85.
40. Noll, D.C., et al., *A homogeneity correction method for magnetic resonance imaging with time-varying gradients.* Medical Imaging, IEEE Transactions on, 1991. **10**(4): p. 629-637.
41. Eddy, W.F., M. Fitzgerald, and D.C. Noll, *Improved image registration by using Fourier interpolation.* Magn Reson Med, 1996. **36**(6): p. 923-31.
42. Cox, R.W. and A. Jesmanowicz, *Real-time 3D image registration for functional MRI.* Magn Reson Med, 1999. **42**(6): p. 1014-8.
43. Lee, C., Grimm, RC, Manduca, A, Felmlee, JP, Ehman, RL, Riederer, SJ, Jack, Jr., CR, *A prospective approach to correct for inter-image head rotation in FMRI.* Magnetic Resonance in Medicine, 1998. **39**(2): p. 234-243.
44. Ward, H.A., et al., *Prospective multiaxial motion correction for fMRI.* Magn Reson Med, 2000. **43**(3): p. 459-69.
45. Welch, E.B., et al., *Spherical navigator echoes for full 3D rigid body motion measurement in MRI.* Magn Reson Med, 2002. **47**(1): p. 32-41.
46. Zhuo, W.F., Wang, Y., Grimm, RC, Rossman, RJ, Felmlee, JP, Riederer, SJ, Ehman, R, *Orbital navigator echoes for motion measurements in magnetic resonance imaging.* Magnetic Resonance in Medicine, 1995. **34**(5): p. 746-753.
47. Tremblay, M., F. Tam, and S.J. Graham, *Retrospective coregistration of functional magnetic resonance imaging data using external monitoring.* Magn Reson Med, 2005. **53**(1): p. 141-9.
48. Speck, O., J. Hennig, and M. Zaitsev, *Prospective real-time slice-by-slice motion correction for fMRI in freely moving subjects.* Magma, 2006. **19**(2): p. 55-61.
49. Kim, B., et al., *Motion correction in fMRI via registration of individual slices into an anatomical volume.* Magn Reson Med, 1999. **41**(5): p. 964-72.
50. Pipe, J.G., *Motion correction with PROPELLER MRI: application to head motion and free-breathing cardiac imaging.* Magn Reson Med, 1999. **42**(5): p. 963-9.
51. Wei, L., F.W. Wehrli, and S. Hee Kwon, *Correcting bulk in-plane motion artifacts in MRI using the point spread function.* Medical Imaging, IEEE Transactions on, 2005. **24**(9): p. 1170-1176.
52. Thesen, S., Heid, Oliver, Mueller, Edgar, Schad, Lothar R. , *Prospective acquisition correction for head motion with image-based tracking for real-time fMRI.* Magnetic Resonance in Medicine, 2000. **44**(3): p. 457-465.

53. Merboldt, K.D., J. Finsterbusch, and J. Frahm, *Reducing inhomogeneity artifacts in functional MRI of human brain activation-thin sections vs gradient compensation.* J Magn Reson, 2000. **145**(2): p. 184-91.
54. Noll, D.C. *Rapid MR image acquisition in the presence of background gradients*. in *Biomedical Imaging, 2002. Proceedings. 2002 IEEE International Symposium on*.2002.
55. Sutton, B.P., D.C. Noll, and J.A. Fessler, *Fast, iterative image reconstruction for MRI in the presence of field inhomogeneities.* IEEE Trans Med Imaging, 2003. **22**(2): p. 178-88.
56. Sutton, B.P., D.C. Noll, and J.A. Fessler, *Dynamic field map estimation using a spiral-in/spiral-out acquisition.* Magn Reson Med, 2004. **51**(6): p. 1194-204.
57. Lund, T.E., et al., *Non-white noise in fMRI: does modelling have an impact?* Neuroimage, 2006. **29**(1): p. 54-66.
58. Woolrich, M.W., et al., *Temporal autocorrelation in univariate linear modeling of FMRI data.* Neuroimage, 2001. **14**(6): p. 1370-86.
59. Johnstone, T., et al., *Motion correction and the use of motion covariates in multiple-subject fMRI analysis.* Hum Brain Mapp, 2006. **27**(10): p. 779-88.
60. Calhoun, V. and T. Adali. *Semi-blind ICA of FMRI: a method for utilizing hypothesis-derived time courses in a spatial ICA analysis*. 2004.
61. Lu, W. and J.C. Rajapakse, *Eliminating indeterminacy in ICA.* Neurocomputing, 2003. **50**: p. 271-290.
62. Blechinger, J.C., E.L. Madsen, and G.R. Frank, *Tissue-mimicking gelatin-agar gels for use in magnetic resonance imaging phantoms.* Med Phys, 1988. **15**(4): p. 629-36.
63. Yang, Y., et al., *Simultaneous perfusion and BOLD imaging using reverse spiral scanning at 3T: characterization of functional contrast and susceptibility artifacts.* Magn Reson Med, 2002. **48**(2): p. 278-89.
64. Glover, G.H. and C.S. Law, *Spiral-in/out BOLD fMRI for increased SNR and reduced susceptibility artifacts.* Magn Reson Med, 2001. **46**(3): p. 515-22.
65. Li, T.Q., et al., *Dual-echo spiral in/in acquisition method for reducing magnetic susceptibility artifacts in blood-oxygen-level-dependent functional magnetic resonance imaging.* Magn Reson Med, 2006. **55**(2): p. 325-34.
66. Noll, D.C., et al., *Deblurring for non-2D Fourier transform magnetic resonance imaging.* Magn Reson Med, 1992. **25**(2): p. 319-33.
67. Truong, T.-K., et al., *Three-dimensional numerical simulations of susceptibility-induced magnetic field inhomogeneities in the human head.* Magnetic Resonance Imaging, 2002. **20**(10): p. 759-770.
68. Ogawa, S., et al., *Intrinsic signal changes accompanying sensory stimulation: functional brain mapping with magnetic resonance imaging.* Proc Natl Acad Sci U S A, 1992. **89**(13): p. 5951-5.
69. Noll, D.C. and W. Schneider. *Theory, simulation, and compensation of physiological motion artifacts in functional MRI*. in *Image Processing, 1994. Proceedings. ICIP-94., IEEE International Conference*. 1994.
70. Hu, X., et al., *Retrospective estimation and correction of physiological fluctuation in functional MRI.* Magn Reson Med, 1995. **34**(2): p. 201-12.

71. Dagli, M.S., J.E. Ingeholm, and J.V. Haxby, *Localization of cardiac-induced signal change in fMRI.* Neuroimage, 1999. **9**(4): p. 407-15.
72. Glover, G.H., T.Q. Li, and D. Ress, *Image-based method for retrospective correction of physiological motion effects in fMRI: RETROICOR.* Magn Reson Med, 2000. **44**(1): p. 162-7.
73. Lund, T.E., et al., *Motion or activity: their role in intra- and inter-subject variation in fMRI.* Neuroimage, 2005. **26**(3): p. 960-4.
74. Lund, T.E., et al., *Non-white noise in fMRI: Does modelling have an impact?* NeuroImage, 2006. **29**(1): p. 54-66.
75. Andersen, A.H., D.M. Gash, and M.J. Avison, *Principal component analysis of the dynamic response measured by fMRI: a generalized linear systems framework.* Magn Reson Imaging, 1999. **17**(6): p. 795-815.
76. Thomas, C.G., R.A. Harshman, and R.S. Menon, *Noise Reduction in BOLD-Based fMRI Using Component Analysis.* NeuroImage, 2002. **17**(3): p. 1521-1537.
77. Martin J. Mckeown, et al., *Analysis of fMRI data by blind separation into independent spatial components.* Human Brain Mapping, 1998. **6**(3): p. 160-188.
78. Martin J. McKeown, et al., *Independent component analysis of fMRI data: Examining the assumptions.* Human Brain Mapping, 1998. **6**(5-6): p. 368-372.
79. Beckmann, C.F. and S.M. Smith, *Probabilistic independent component analysis for functional magnetic resonance imaging.* Medical Imaging, IEEE Transactions on, 2004. **23**(2): p. 137-152.
80. Aapo Hyvarinen, J.K., Erkki Oja, *Independent Component Analysis*. 1st ed. 2001, New York: Wiley. 481.
81. Calhoun, V.D. and T. Adali, *Unmixing fMRI with independent component analysis.* Engineering in Medicine and Biology Magazine, IEEE, 2006. **25**(2): p. 79-90.
82. Hyvarinen, A., *Fast and robust fixed-point algorithms for independent component analysis.* Neural Networks, IEEE Transactions on, 1999. **10**(3): p. 626-634.
83. Hesse, C.W. and C.J. James, *The FastICA algorithm with spatial constraints.* Signal Processing Letters, IEEE, 2005. **12**(11): p. 792-795.
84. Wei, L. and J.C. Rajapakse, *Approach and applications of constrained ICA.* Neural Networks, IEEE Transactions on, 2005. **16**(1): p. 203-212.
85. Calhoun, V.D., et al., *Semi-blind ICA of fMRI: A method for utilizing hypothesis-derived time courses in a spatial ICA analysis.* Neuroimage, 2005. **25**(2): p. 527-538.
86. James, C.J. and O.J. Gibson, *Temporally constrained ICA: an application to artifact rejection in electromagnetic brain signal analysis.* Biomedical Engineering, IEEE Transactions on, 2003. **50**(9): p. 1108-1116.
87. Noll, D.C., et al., *Estimating test-retest reliability in functional MR imaging. II: Application to motor and cognitive activation studies.* Magn Reson Med, 1997. **38**(3): p. 508-17.
88. Koch, K.M., et al., *Sample-specific diamagnetic and paramagnetic passive shimming.* J Magn Reson, 2006. **182**(1): p. 66-74.
89. Marques, J., Bowtell, R, *Application of a Fourier-based method for rapid calculation of field inhomogeneity due to spatial variation of magnetic*

susceptibility. Concepts in Magnetic Resonance Part B: Magnetic Resonance Engineering, 2005. **25B**(1): p. 65-78.